GOBAI-O₂: temporally and spatially resolved fields of ocean interior dissolved oxygen over nearly two decades

Jonathan D. Sharp[1,2], Andrea J. Fassbender[2], Brendan R. Carter[1,2], Gregory C. Johnson[2], Cristina Schultz[3,4], John P. Dunne[3]

[1]Cooperative Institute for Climate, Ocean, and Ecosystem Studies, University of Washington, Seattle, WA, 98105, United States

[2]Pacific Marine Environmental Laboratory, National Oceanic and Atmospheric Administration, Seattle, WA, 98115, United States

[3]Geophysical Fluid Dynamics Laboratory, National Oceanic and Atmospheric Administration, Princeton, NJ, 08540, United States

[4]Princeton University, Princeton, NJ, 08540, United States

Correspondence to: Jonathan D. Sharp (jonathan.sharp@noaa.gov)

Abstract. Over a decade ago, oceanographers began installing oxygen sensors on Argo profiling floats to be deployed throughout the world ocean, with the stated objective of better constraining trends and variability in the ocean's inventory of oxygen. Until now, measurements from these Argo-mounted oxygen sensors have been mainly used for localized process studies on air–sea oxygen exchange, upper ocean primary production, biological pump efficiency, and oxygen minimum zone dynamics. Here we present a four-dimensional gridded product of ocean interior oxygen, derived via machine learning algorithms trained on dissolved oxygen observations from Argo-mounted sensors and discrete measurements from ship-based surveys, and applied to temperature and salinity fields constructed from the global Argo array. The data product is called GOBAI-O₂ for Gridded Ocean Biogeochemistry from Artificial Intelligence – Oxygen (Sharp et al., 2023; https://doi.org/10.25921/z72m-yz67; last access: 19 Mar. 2023); it covers 86% of the global ocean area on a 1° latitude by 1° longitude grid, spans the years 2004–2022 with monthly resolution, and extends from the ocean surface to two kilometers in depth on 58 levels. Two types of machine learning algorithms — random forest regressions and feed-forward neural networks — are used in the development of GOBAI-O₂, and the performance of those algorithms is assessed using real observations and simulated observations from Earth system model output. GOBAI-O₂ is evaluated through comparisons to the oxygen climatology from the World Ocean Atlas, the mapped oxygen product from the Global Ocean Data Analysis Project, and direct observations from large-scale hydrographic research cruises. Finally, potential uses for GOBAI-O₂ are demonstrated by presenting average oxygen fields on isobaric and isopycnal surfaces, average oxygen fields across vertical–meridional sections, climatological seasonal cycles of oxygen averaged over different pressure intervals, and globally integrated time series of oxygen. GOBAI-O₂ indicates that the oxygen inventory in the upper two kilometers of the global ocean has been declining by about 0.71 ± 0.13 % dec.$^{-1}$ between 2004 and 2022.

1 Introduction

The inventory of dissolved oxygen in the global ocean has been declining over recent decades and is projected to continue to decline through the current century (Keeling et al., 2010; Breitburg et al., 2018; Bindoff et al., 2019; Stramma and Schmidtko, 2019; Limburg et al., 2020), leading to detrimental consequences for aerobic marine organisms (Pörtner and Farrell, 2008; Sampaio et al., 2021) and changes to biogeochemical cycles, potentially triggering important climatological feedbacks (Gruber, 2004; Berman-Frank et al., 2008). Historical deoxygenation has been inferred from analyses of globally distributed observations (Helm et al., 2011; Schmidtko et al., 2017; Ito et al., 2017) and has been reproduced in Earth system model (ESM) reconstructions (Bopp et al., 2013; Frölicher et al., 2009; Kwiatkowski et al., 2020). Global observational studies have generally indicated a greater degree of deoxygenation than model studies over recent decades, indicating that ESMs may misrepresent the sensitivities of the physical and biological processes leading to deoxygenation, which has implications for the reliability of future projections (Oschlies et al., 2017; 2018; Stramma and Schmidtko, 2021). Model studies, however, are based on gridded output that is continuously resolved in space and time, whereas observational studies rely on interpolation of measurements from discrete bottle samples and/or profiling sensors. These observational datasets have significant spatiotemporal gaps and may not robustly represent global deoxygenation trends.

Discrete measurements of dissolved oxygen concentration ($[O_2]$) are typically made using Winkler titrations (Winkler, 1888; Carpenter, 1965; Langdon, 2010), which are also used to calibrate measurements from electrode (or more recently sometimes optical) dissolved oxygen sensors mounted on Conductivity-Temperature-Depth (CTD) profilers. Globally distributed $[O_2]$ observations from discrete measurements and CTD profilers have been provided by hydrographic programs like the World Ocean Circulation Experiment (WOCE), the Climate and Ocean: Variability, Predictability and Change (CLIVAR) program, and the Global Ocean Ship-Based Hydrographic Investigations Program (GO-SHIP). Data from these programs are publicly available and are conveniently compiled into databases such as the World Ocean Database (WOD; Boyer et al., 2018) and the Global Ocean Data Analysis Project (GLODAP; Lauvset et al., 2022). Though unprecedented spatial coverage is provided by global hydrographic programs, the decadal-scale temporal resolution of WOCE, CLIVAR, and GO-SHIP data precludes robust analyses of year-to-year and/or seasonal variability in $[O_2]$.

Since the mid-2000s, approximately 1,800 Argo floats equipped with oxygen sensors have been deployed. Argo floats profile the upper ~2000 meters of the water column every ~10 days. Many oxygen-equipped Argo floats have been deployed as parts of regional arrays such as the Southern Ocean Carbon and Climate Observations and Modeling (SOCCOM; soccom.princeton.edu) project and the North Atlantic Aerosols and Marine Ecosystems Study (NAAMES; science.larc.nasa.gov/NAAMES/). More recently, the push for a global biogeochemical Argo array has spurred the deployment of oxygen-equipped Argo floats into more sparsely sampled ocean regions (Johnson and Claustre, 2016; Claustre et al., 2020). As more floats have been deployed, improvements have been made to sensor calibration, data adjustments, and quality control.

Notably, pre-deployment drift corrections (D'Asaro and McNeil, 2013; Johnson et al., 2015; Bittig and Körtzinger, 2015; Bushinsky et al., 2016; Drucker and Riser, 2016; Nicholson and Feen, 2017), climatology-based calibrations (Takeshita et al., 2013), calibrations via in-air oxygen measurements (Körtzinger et al., 2005; Fiedler et al., 2013; Bittig and Körtzinger, 2015; Johnson et al., 2015; Bushinsky et al., 2016), post-deployment drift corrections (Johnson et al., 2017; Bittig et al., 2018a), and well-established procedures for delayed-mode quality control (Maurer et al., 2021) have substantially reduced the uncertainty and increased the reproducibility of optode-based $[O_2]$ measurements on Argo floats.

From the time it began, the Argo-Oxygen program (now oxygen is a measured variable under the Biogeochemical Argo program) intended to document ocean deoxygenation, predict and assess anoxic and hypoxic events, and determine seasonal to interannual changes in export production (Gruber et al., 2010). Until now, these goals have been achieved primarily on a regional scale. For example, $[O_2]$ measurements from biogeochemical Argo floats have been used to examine ventilation and air–sea exchange of oxygen in the Southern Ocean (Bushinsky et al., 2017) and during Deep Water formation in the Subpolar North Atlantic (Körtzinger et al., 2004; Piron et al., 2016; 2017; Wolf et al., 2018); denitrification and the spatial extent of the oxygen minimum zone in the Bay of Bengal (Sarma and Udaya Bhaskar, 2018; Johnson et al., 2019; Udaya Bhaskar et al., 2021); and carbon production and export in the Pacific Ocean (Bushinsky and Emerson, 2015, 2018; Yang et al., 2017), Southern Ocean (Stukel and Ducklow, 2017; Arteaga et al., 2019), and North Atlantic Ocean (Alkire at al., 2012; Estapa et al., 2019). Recently, in an early global-scale analysis of $[O_2]$ from the Argo array, Johnson and Bif (2021) used the diel cycle of oxygen measured by the ocean-wide array of biogeochemical Argo floats to constrain net primary production in the surface ocean.

With the work presented here, we seek to capitalize on the collective efforts of global hydrographic programs, Biogeochemical Argo, and Core Argo to create a first-of-its-kind data product: a four-dimensional monthly record of dissolved oxygen in the global ocean. We combine autonomous observations of $[O_2]$ from BGC Argo floats with discrete observations of $[O_2]$ from hydrographic cruises in the GLODAP database to create a dataset with extensive spatial and temporal resolution. With this dataset, we train machine learning (ML) algorithms on ocean interior predictor variables co-located with $[O_2]$ observations; evaluate those algorithms using real and simulated data; and apply the algorithms to gridded ocean interior predictor variables mapped from Core Argo to produce a gridded $[O_2]$ data product at a monthly resolution from 2004–2022, on 58 pressure levels in the upper two kilometers of the ocean, and on a near-global 1° latitude by 1° longitude grid.

In this paper, we present the four-dimensional gridded $[O_2]$ product — which we call GOBAI-O_2 (Gridded Ocean Biogeochemistry from Artificial Intelligence – Oxygen; Sharp et al., 2023; https://doi.org/10.25921/z72m-yz67; last access: 19 Mar. 2023) — analyzing spatial patterns, seasonal cycles, and decadal variability. We discuss the process for creating GOBAI-O_2, show the results of evaluation exercises, assess uncertainty in the gridded $[O_2]$ fields, and compare the data product to other gridded datasets and discrete measurements. GOBAI-O_2 represents the first step in leveraging the emerging global

3

array of BGC Argo floats to produce spatially-resolved, time-varying snapshots of global ocean biogeochemical distributions in near real-time. Critically, GOBAI-O_2 can be used to address the goals of the Argo-Oxygen program set by Gruber et al. (2010) over a decade ago, providing regional and global insight into ocean deoxygenation and hypoxia on timescales ranging from a few months to multiple years.

## 2 Methods

2.1 Data sources and processing

Hydrographic cruise data were obtained from the GLODAP version 2022 data product (GLODAPv2.2022; Key et al., 2015; Olsen et al., 2016; Lauvset et al., 2022). GLODAPv2.2022 provides quality-controlled data from throughout the entire water column obtained via discrete analyses of more than 1.4 million water samples collected on 1,085 research cruises. Discrete Winkler titration data were chosen rather than CTD oxygen profiles due to the issues with the quality of calibration of some CTD oxygen measurements and the relatively coarse vertical resolution of the final GOBAI-O_2 product, which would not benefit from the high vertical resolution of CTD profiles. Furthermore, the additional resolution would slow the GOBAI-O_2 algorithm training process. Data from GLODAP were chosen rather than data from the WOD or any other database due to the high degree of quality control applied to GLODAP data. Dissolved oxygen is the most represented biogeochemical variable in GLODAPv2.2022, with more than 1.2 million data points from 991 research cruises. Data from GLODAPv2.2022 were filtered to retain only samples collected after 1 Jan. 2004, from 0 to 2500 decibars (dbars), and with a quality-control flag of 1 (meaning the data were manually inspected) and quality flags of 2 (good) for both salinity and [O_2]. Temperature is not assigned either flag and is assumed to be of sufficient quality if it is reported (Lauvset et al., 2022). This filtering left 450,032 data points from 21,513 unique profiles from 393 total cruises (red points in Fig. 1).

Float data were obtained from synthetic profile ("Sprof") files (Bittig et al., 2022) stored in the Argo Global Data Assembly Centres (GDACs) via the OneArgo-Mat toolbox (Frenzel et al., 2022) for MATLAB (MathWorks). At the time data were obtained (03 Mar. 2023), the Argo GDACs contained data from 1,780 floats equipped with [O_2] sensors. Float data were filtered to retain only delayed-mode-adjusted data with quality flags of 1 (good), 2 (probably good), or 8 (interpolated/extrapolated) for pressure, temperature, salinity, and [O_2]. This filtering ensured float data had been manually reviewed by a data manager and assigned an appropriate quality flag. This filtering left 26,671,557 data points from 133,488 unique profiles from 972 total floats (blue points in Fig. 1).

The discrete temperature, salinity, and [O_2] data obtained from GLODAPv2.2022 and the Argo GDACs are archived online (Appendix C; https://doi.org/10.5281/zenodo.7747237). To ensure the trained machine learning algorithms were not biased toward BGC Argo float data, which in their native format have higher vertical resolution than GLODAP data, each profile was interpolated to, at most, 58 standard depth levels (the same depth levels on which the final GOBAI-O_2 data product is provided).

Interpolated temperature, salinity, and [O_2] data from each source are also archived online (Appendix C; https://doi.org/10.5281/zenodo.7747237). After interpolation, the total number of GLODAP data points used for algorithm training increased to 1,096,324 and the total number of Argo float data points used for algorithm training decreased to 6,480,283. Co-located, interpolated GLODAP and BGC Argo profiles that fell within the same $1° \times 1°$ monthly, depth-dependent grid cells were compared for internal consistency. The float [O_2] values were adjusted according to the procedure in Appendix D to remove the small global discrepancy between co-located ship and float measurements to ensure internal consistency between the two datasets.
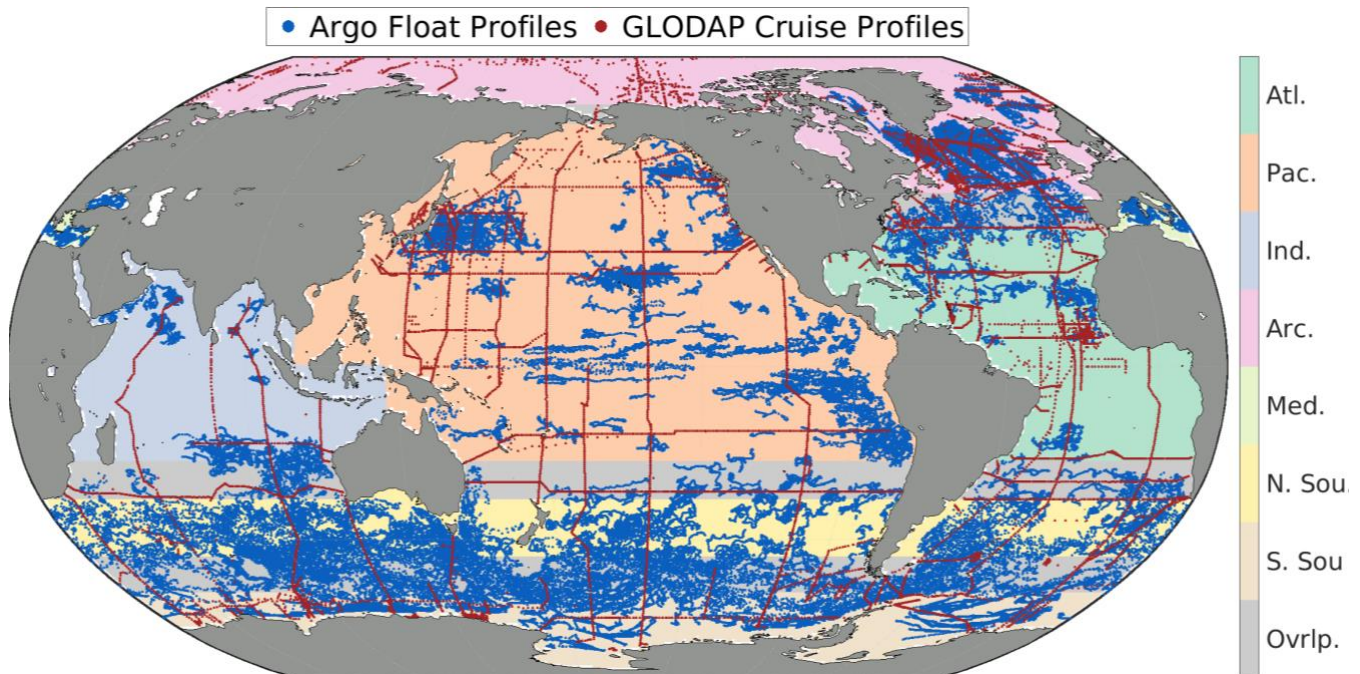
Figure 1: Discrete profile locations from oxygen-equipped Argo floats (blue) and GLODAPv2.2022 cruises (red) from 1 Jan. 2004 to 3 Mar. 2023. Data from these profiles were binned and used to train ML algorithms to estimate [O_2] in each of seven regions: the Atlantic Ocean (Atl.), Pacific Ocean (Pac.), Indian Ocean (Ind.), Arctic Ocean (Arc.), Mediterranean Sea (Med.), northern section of the Southern Ocean (N. Sou.), and southern section of the Southern Ocean (S. Sou.). Overlapping areas between regions are shown in grey (Ovrlp.), where [O_2] estimates are made by taking distance-weighted averages of outputs from two regional ML algorithms. The regional boundaries are presented in numerical form in Table B1.

BGC Argo float and GLODAP cruise data were combined into a single dataset after this bias adjustment, which will be referred to as the "combined dataset" from here on. The combined dataset was grouped into seven overlapping regions (Fig. 1, Table B1). This grouping was intended to account implicitly for similar physical–biogeochemical relationships within large ocean regions and to reduce the computational burden of the machine learning (ML) algorithm fits described below. The regions were initially chosen to imitate the biomes presented by Fay and McKinley (2014), and were then expanded to relatively large

5

150 regions bound either by land masses or by overlapping boundaries along constant lines of latitude. The number of profiles made within each $1° \times 1°$ box by either a discrete ship cast or Argo float (supplementary material, Fig. A1) provides a measure of the temporal resolution of the combined dataset in addition to the spatial distribution shown in Fig. 1.

Gridded temperature and salinity data to which the trained algorithms were applied were obtained from the latest version of
155 the Roemmich and Gilson (2009) (RG09) Argo Climatology (https://sio-argo.ucsd.edu/RG_Climatology.html; last access: 12 Jan. 2023). The RG09 climatology is an upper ocean (0–2000 dbar) gridded temperature and salinity product constructed exclusively from Argo observations. Long-term (2004–2018) mean fields of temperature and salinity are provided on 58 depth levels, along with monthly anomaly fields on each of those depth levels from 2004 to the present day. The most recent major update of the RG09 climatology was made in 2019, and new monthly anomaly fields are provided in near-real-time between
160 major updates. Monthly gridded temperature and salinity were calculated from the RG09 long-term mean and monthly anomaly fields (Fig. A2), then used for the creation of the gridded [O_2] product discussed below.

Output from the NOAA Geophysical Fluid Dynamics Laboratory's Earth System Model Version 4 (GFDL-ESM4; Dunne et al., 2020) was used to assess algorithm performance. Model output was downloaded from the World Climate Research
165 Programme database (https://esgf-node.llnl.gov/projects/cmip6/; last access: 8 Apr. 2022), which hosts data from models participating in the sixth phase of the Coupled Model Intercomparison Project (CMIP6). Potential temperature, practical salinity, and [O_2] were downloaded to coincide with available ocean interior observations (Fig. A3). Historical outputs (2004–2014) and projected outputs under SSP2-4.5 (2015–2022) were combined to cover the time period over which observations were available. A spatial mask was applied to retain only GFDL-ESM4 grid cells with corresponding temperature and salinity
170 values in the RG09 climatology, because that is the final grid on which GOBAI-O_2 is produced.

2.2 Algorithm training

The combined dataset was used to train ML algorithms for each region to estimate [O_2] from absolute salinity, conservative temperature, potential density anomaly, hydrostatic pressure, bottom depth, and additional spatiotemporal information to allow for geographic, seasonal, and interannual variation (see Table 1). Though biology is not explicitly accounted for in the ML
175 algorithms, Giglio et al. (2018) demonstrate that, with an appropriately distributed dataset, the inclusion of spatiotemporal variables in algorithm training can implicitly accommodate biological processes.

Absolute salinity (S_A) was calculated from practical salinity (S_P), hydrostatic pressure (P), latitude, and longitude. Conservative temperature (θ) was calculated from in situ temperature (T), S_A, and P. Potential density anomaly (σ_θ) was calculated from S_A
180 and θ. These calculations were made using the Gibbs-SeaWater (GSW) Oceanographic Toolbox for MATLAB (McDougall and Barker, 2011). As was done by Carter et al. (2021), longitude was transformed into two separate predictors: cos(Longitude − 20° E) and cos(Longitude − 110° E). Cosine functions were applied to maintain the cyclical nature of longitude as a predictor,

6

and offsets of 20° E and 110° E were intended to shift regions where the cosine function has minimum explanatory power over landmasses. Bottom depth was determined by matching each observational location with the corresponding bathymetry from the ETOPO2v2 global relief model (NOAA National Geophysical Data Center, 2006).

Table 1. Predictor variables used to train random forest regressions and feed-forward neural networks to predict $[O_2]$.

Predictor Variable	Abbreviation	Unit	Range (approx.)
Conservative Temperature	θ	°C	−2 to 32
Absolute Salinity	S_A	N/A	14 to 40
Potential Density Anomaly	σ_θ	kg m^{-3}	9.3 to 29.3
Hydrostatic Pressure	P	dbar	0 to 2000
Latitude	lat	°	−78 to 90
cos(Longitude – 20°)	lon_{cos20}	N/A	−1 to 1
cos(Longitude – 110°)	lon_{cos110}	N/A	−1 to 1
Bottom depth	bot	meters	0 to 10,000
Year	yr	years	2004 to 2023
sin(2π · Day of Year / 365.25)	doy_{sin}	N/A	−1 to 1
cos(2π · Day of Year / 365.25)	doy_{cos}	N/A	−1 to 1

Two types of ML algorithms were trained: feed-forward neural networks (FNNs; Demuth et al., 2008) and random forest regressions (RFRs; Breiman, 2001), each of which were trained on the input variables given in Table 1 to produce estimates of $[O_2]$ (Fig. A4). Three separate FNNs were trained for each of the seven basins shown in Fig. 1, with an average of the three taken to obtain one equally weighted FNN result. The FNNs were constructed using the "feedforwardnet" function and trained using the "train" function, both from Version 14.4 of the Deep Learning Toolbox for MATLAB (R2022a). Each FNN was trained using a Levenberg-Marquardt algorithm, with 15% of the data reserved for testing the network during training steps. Each FNN had two hidden layers, with the following combinations of neurons in the first and second layer, respectively: 20 and 10, 15 and 15, and 10 and 20. One RFR was trained for each of the seven basins shown in Fig. 1. RFRs are ensembles of decision trees, each created with a bootstrapped version of the full dataset chosen randomly with replacement. Each RFR consisted of 600 trees, a minimum leaf size of 5, and six of the eleven predictors used for each decision split. These parameters were chosen after some trial and error to strike a balance between computational efficiency and algorithm performance. The MATLAB "treebagger" function was used to train RFRs.

In areas where two regions overlap (see Fig. 1), weighted averages of $[O_2]$ estimates were calculated in overlapping grid cells from each regional algorithm. These averages were weighted by distance from the center latitude line of the overlapping area (e.g., a point at 33 °S in the overlapping area between the N. Sou. region (whose northern border extends to 25 °S) and the Atl. region (whose southern border extends to 35 °S) would be calculated as $[O_2] = 0.8[O_2]_{N.Sou.} + 0.2[O_2]_{Atl.}$). Overlapping areas were used to mitigate discontinuities at the boundaries between regions in the final gridded product.

The average of FNN and RFR estimates (ENS, for ensemble average) was used as the $[O_2]$ estimate for a given set of input data. This ensemble averaging procedure was implemented due to insights from previous work showing that averaging the outputs of multiple ML algorithms or linear regression models often outperforms the output from just one approach on its own (Gregor et al., 2017; 2019; Bittig et al., 2018b; Carter et al., 2021; Djeutchouang et al., 2022), likely due to complementary strengths and weaknesses of each approach. For this work, any especially erroneous result from either the FNN or RFR should be mitigated by better results from the other algorithm.

2.3 Algorithm evaluation

We performed two exercises to evaluate the effectiveness of the ML algorithms used to estimate $[O_2]$. The first exercise involved training separate evaluation algorithms ($RFR_{Data-Eval}$ and $FNN_{Data-Eval}$ algorithms) as described in section 2.2 using a subset of the observational dataset for training while reserving the remaining subset for assessment. For this exercise, data were split randomly into training (80%) and assessment (20%) groups; this split was made according to measurement platform (cruise or float; see Fig. A5) to ensure that inherent correlations among the data points from a single cruise or float did not contribute to the apparent effectiveness of each ML algorithm. Then $[O_2]$ values from the subset of reserved assessment data were compared to estimates of $[O_2]$ from $RFR_{Data-Eval}$, $FNN_{Data-Eval}$, and the ensemble average of the two ($ENS_{Data-Eval}$). This exercise was intended to evaluate the ability of the ML algorithms to reproduce measured data that was not involved in algorithm training (section 3.1.1).

The second exercise involved training evaluation algorithms ($RFR_{ESM4-Eval}$ and $FNN_{ESM4-Eval}$ algorithms) using synthetic "profiles" extracted from gridded GFDL-ESM4 output at the times and locations where observational data were available, then assessing the evaluation algorithms using spatially and temporally continuous monthly GFDL-ESM4 output from 2004 through 2022. For this exercise, synthetic profiles for algorithm training were defined by matching the latitude, longitude, month, and year of each available grid cell from the binned observational dataset with the corresponding GFDL-ESM4 output. This resulted in 74,589 synthetic profiles for algorithm training. $RFR_{ESM4-Eval}$ and $FNN_{ESM4-Eval}$ algorithms were trained as described in section 2.2 with the synthetic training data, then used to produce $[O_2]$ estimates for the complete model output. These $[O_2]$ estimates from $RFR_{ESM4-Eval}$, $FNN_{ESM4-Eval}$, and an ensemble average of the two ($ENS_{ESM4-Eval}$) were compared to $[O_2]$ values from the full GFDL-ESM4 output fields at the grid-cell level. This exercise was intended to evaluate the ability of the ML algorithms to estimate $[O_2]$ in a spatiotemporally resolved Earth system model environment when limited to training data representative of the available collection of ocean oxygen observations (section 3.1.2). The four-dimensional field of $[O_2]$ from $ENS_{ESM4-Eval}$ that represents a reconstruction of the GFDL-ESM4 environment, which we refer to as GOBAI-O_2-ESM4, can also be used as an analogue for how well GOBAI-O_2 (trained on real observational data, section 2.4) might represent $[O_2]$ variability in the real-world environment. For this reason, the four-dimensional field of differences between GOBAI-O_2-ESM4 and GFDL-ESM4 output were used to inform the evaluation of GOBAI-O_2 uncertainty (sections 2.5 and 3.2.4). Additionally, we quantified global means, seasonal cycle amplitudes, long-term trends, and interannual variabilities in $[O_2]$ across different

depth intervals of GOBAI-O$_2$-ESM4. To evaluate the performance of GOBAI-O$_2$-ESM4 on a global scale, these metrics are compared to the same metrics for the spatiotemporally resolved GFDL-ESM4 output and subsampled grid cells in GFDL-ESM4 corresponding to observational data coverage (section 3.1.2). Comparisons of global means from GOBAI-O$_2$-ESM4 to GFDL-ESM4 are also used to approximate uncertainty in oxygen inventories for the assessment of trends (section 3.2.3).

2.4 Creation of GOBAI-O$_2$

FNNs and RFRs for each of the seven regions shown in Fig. 1 were trained with the full combined dataset, using the predictor variables shown in Table 1, with [O$_2$] as a target variable. Then, the FNNs and RFRs were applied to S_A, θ, and σ_θ calculated from RG09 temperature and salinity fields, along with spatiotemporal information from RG09 grid cells. Weighted averages were calculated where regions overlapped, and ensemble averages (ENS) were calculated from the FNN and RFR estimates. This produced a monthly gridded [O$_2$] product in the upper two kilometers of the ocean on a global grid from January 2004 to December 2022, i.e. GOBAI-O$_2$ (Sharp et al., 2022; https://doi.org/10.25921/z72m-yz67; last access: 19 Mar. 2023; sections 3.2.1–3.2.3). GOBAI-O$_2$ was compared to gridded climatological oxygen fields from the 2018 World Ocean Atlas (WOA18; Garcia et al., 2019; section 3.2.5), the GLODAP mapped data product (Lauvset et al., 2016; section 3.2.5), and discrete measurements of oxygen from select cruises between 2004 and 2022 (section 3.2.6).

2.5 Uncertainty estimation

Similar to previous studies that have estimated uncertainty in observation-based biogeochemical data products (e.g., Landschützer et al., 2014; Gregor and Gruber, 2021; Keppler et al., 2020; under review), we combine uncertainty from three separate sources — measurement, gridding, and algorithm — to estimate uncertainty in GOBAI-O$_2$ (section 3.2.4).

Measurement uncertainty ($u([O_2])_{meas.}$) is attributable to the [O$_2$] observations themselves. For this quantity, gridded [O$_2$] from GOBAI-O$_2$ is multiplied by 1.5%, which is between the nominal value for the consistency of the GLODAPv2.2022 cruise dataset — stated to be 1% (Lauvset et al., 2022) — and the approximate accuracy of BGC Argo float observations — estimated as about 3 μmol kg^{-1} (Johnson et al., 2017; Maurer et al., 2021), which is close to 2% of average ocean [O$_2$]. We recognize, however, that even 2% is a rather optimistic estimate for the accuracy of float [O$_2$] sensors, especially when crossing large vertical gradients (Bittig and Körtzinger, 2017; Bittig et al., 2018a). On a related note, no temporal lag corrections were applied to our float [O$_2$] dataset (Bittig et al., 2014; Bittig and Körtzinger, 2017).

Gridding uncertainty ($u([O_2])_{grid.}$) is attributable to using a single [O$_2$] value to represent a four-dimensional box that is coarser in time and space than the resolution of many processes that influence [O$_2$]. We estimate gridding uncertainty by (1) binning the combined GLODAP and Argo observational dataset to grid cells equal in size to the RG09 grid cells; (2) calculating the standard deviation among the observations in cells with more than ten observations (Fig. A6); (3) fitting a multivariate polynomial regression relating those standard deviations to depth, potential density anomaly, and bottom depth; and (4)

9

applying that regression to the RG09 grid to compute an estimated standard deviations (i.e., gridding uncertainty) in each grid cell.

275

Algorithm uncertainty ($u([O_2])_{alg.}$) is attributable to the ML algorithms that estimate [O$_2$] on the RG09 grid. We estimate algorithm uncertainty using the four-dimensional field of absolute differences between [O$_2$] from GFDL-ESM4 model output versus GOBAI-O$_2$-ESM4, determined from the GFDL-ESM4 algorithm evaluation exercise described in section 2.3.

280

The three uncertainty sources were combined in quadrature (assuming independence) to calculate a combined uncertainty estimate for each gridded [O$_2$] value in GOBAI-O$_2$ ($u([O_2])_{tot.}$):

$$u([O_2])_{tot.} = \sqrt{u([O_2])^2_{meas.} + u([O_2])^2_{grid.} + u([O_2])^2_{alg.}} \tag{1}$$

3 Results and Discussion

3.1 Algorithm evaluation

The evaluation exercises indicated that the ML algorithms trained on the combined GLODAP and Argo observational dataset were effective in their ability to estimate [O$_2$] and reconstruct seasonal to decadal variability in the global oxygen inventory. Mean offsets ($\Delta[O_2] = [O_2]_{obs/mod} - [O_2]_{est}$) and root mean squared differences (RMSDs) between [O$_2$] from direct measurements ([O$_2$]$_{obs}$) or GFDL-ESM4 output ([O$_2$]$_{mod}$) and [O$_2$] estimated from ML algorithms ([O$_2$]$_{est}$) were determined as an assessment of the ability of the algorithms to estimate [O$_2$] at a grid-cell level (Table 2; Fig. 2; Tables B2– B4). Mean $\Delta[O_2]$ and RMSD determined using [O$_2$]$_{est}$ from the ESPER-Mixed model (Carter et al., 2021) — an average of predictions from a neural network and moving window multiple linear regression trained on GLODAPv2.2020 data — were also determined as a point of comparison for the observational data-based validation test (Table 2; Fig. A7; Table B4). In the case of the GFDL-ESM4-based validation test, metrics to summarize means, amplitudes, trends, and variability in integrated mean [O$_2$] values were determined to demonstrate the ability of the GOBAI-O$_2$ method to capture seasonal to decadal scale variability in oxygen at the global scale (Table 3; Fig. 3). The results of each evaluation exercise are discussed in more detail in the following sections.
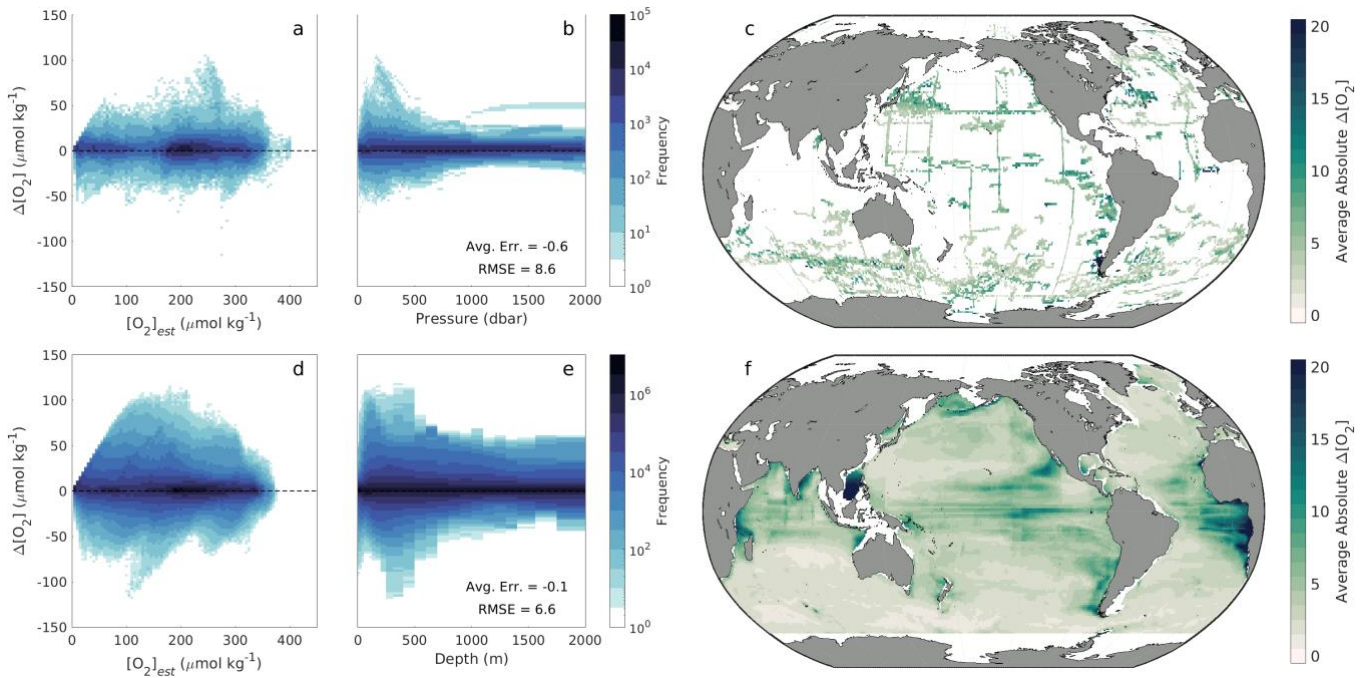
3.1.1 Test with withheld observational data

Estimates of [O$_2$] using ENS$_{Data-Eval}$ algorithms tracked closely with [O$_2$]$_{obs}$ and showed no strong systematic biases with [O$_2$]$_{est}$ or depth (Fig. 2a and 2b), though variability in $\Delta[O_2]$ was greatest from just below the surface to about 500 dbars. Mean offsets were between −2.0 and 0.2 µmol kg^{-1} for the seven regions, with a global average of −0.6 µmol kg^{-1}; RMSDs were between 7.3 and 9.1 µmol kg^{-1} for the seven regions, with a global average of 8.6 µmol kg^{-1} (Table 2). The slightly negative global

10

average offset suggests somewhat higher estimated than measured [O$_2$] values, and the lowest RMSDs from the ENS$_{\text{Data-Eval}}$ algorithms were found in the southern section of the Southern Ocean (Table 2 and Fig. 2c). However, this evaluation exercise is influenced by the incomplete subset of data (20%) used to test the ENS$_{\text{Data-Eval}}$ algorithms. A cross-fold validation (i.e., repeating this exercise with five separate 20% chunks of data withheld from algorithm training) was prohibitively computationally expensive. Therefore, the associated Δ[O$_2$] and RMSD values alone are not as instructive as a comparison to the Δ[O$_2$] and RMSD values obtained from the ESPER-Mixed model (Table 2).

Table 2. Regional and global error statistics (mean Δ[O$_2$] and RMSD) for evaluation exercises using the ensemble average (ENS$_{\text{Data-Eval}}$) of FNN$_{\text{Data-Eval}}$ and RFR$_{\text{Data-Eval}}$ algorithms trained on a subset of data from the combined GLODAP and Argo observational dataset and tested with a separate subset of withheld data, or the ensemble average (ENS$_{\text{ESM4-Eval}}$) of FNN$_{\text{ESM4-Eval}}$ and RFR$_{\text{ESM4-Eval}}$ algorithms trained on a subset of output from GFDL-ESM4 (corresponding to locations of available Argo and GLODAP data) and tested using the full field of GDFL-ESM4 output. Error statistics calculated using the ESPER-Mixed model are also shown for comparison to the data-based test. The numbers of data points used in the training and assessment of each algorithm are shown.

| Basin | Evaluation Exercise with Observational Data | | | | | | Evaluation Exercise with GFDL-ESM4 Output | | | |
| | Training Data Points | Assessment Data Points | ENS$_{\text{Data-Eval}}$ | | ESPER-Mixed | | Training Data Points | Assessment Data Points | ENS$_{\text{ESM4-Eval}}$ | |
			Mean Δ[O$_2$] (µmol kg^{-1})	RMSD (µmol kg^{-1})	Mean Δ[O$_2$] (µmol kg^{-1})	RMSD (µmol kg^{-1})			Mean Δ[O$_2$] (µmol kg^{-1})	RMSD (µmol kg^{-1})
Atl.	553,272	131,488	−1.2	8.4	−3.1	11.1	179,322	28,235,064	−0.7	9.0
Pac.	1,692,647	533,165	−0.1	9.1	−3.9	13.8	522,834	69,369,456	−0.1	7.5
Ind.	365,977	50,906	−1.6	7.8	−2.5	10.2	85,748	20,736,144	0.3	6.9
Arc.	919,361	93,191	0.2	8.4	−1.4	11.3	281,684	11,547,744	−0.1	4.2
Med.	202,690	45,749	−2.0	7.8	−3.5	13.2	32,110	1,096,680	1.0	5.5
N. Sou.	2,125,988	573,925	−0.9	8.3	−2.9	10.6	752,856	67,626,624	−0.1	4.3
S. Sou.	1,399,346	374,952	−0.3	7.3	−2.4	10.9	515,502	31,412,472	0.0	3.3
Global	7,259,281	1,803,376	−0.6	8.6	−3.1	12.1	2,370,056	230,024,184	−0.1	6.6

Estimates of [O$_2$] using ESPER-Mixed (Fig. A7) showed average offsets between −3.9 and −1.4 µmol kg^{-1} for the seven regions (with a global average of −3.1 µmol kg^{-1}) and RMSDs between 10.2 and 13.8 µmol kg^{-1} for the seven basins (with a global average of 12.1 µmol kg^{-1}) (Table 2). Again, the negative global average offset suggests higher estimated than measured [O$_2$] values. Compared to ESPER-Mixed (Carter et al., 2021), the ENS$_{\text{Data-Eval}}$ algorithms performed better, both in terms of Δ[O$_2$] and RMSD in each individual region and overall. This result is likely a reflection of the fact that ENS$_{\text{Data-Eval}}$ algorithms were trained with more varied data than the ESPER-Mixed model (Argo and GLODAP compared to just GLODAP), and that the withheld data for which estimates were made also comprised more varied data (both Argo and GLODAP as well). Importantly, when estimates were made for just the GLODAP dataset, the ENS$_{\text{Data-Eval}}$ algorithms still performed better than ESPER-Mixed (Table B4), suggesting that the seasonally-resolved float data supply important information to the relationships established during algorithm training.

Figure 2. (a,b,d,e) Two-dimensional histograms showing offsets between measured versus estimated oxygen ($\Delta[O_2] = [O_2]_{obs} - [O_2]_{est}$) for (a,b) withheld observational data and (d,e) modeled versus estimated oxygen ($\Delta[O_2] = [O_2]_{mod} - [O_2]_{est}$) for GFDL-ESM4 model output as a function of (a,d) $[O_2]_{est}$ and (b,e) depth in the water column. Offsets are binned into cells that are 2.5 µmol kg^{-1} tall in terms of $\Delta[O_2]$ and (a,d) 5 µmol kg^{-1} wide in terms of $[O_2]_{est}$ or equivalent in width to (b) the interpolated depth levels of the data or (e) the vertical resolution of GFDL-ESM4 grid cells. The frequency of offsets that fall into a given bin is shown on a logarithmic scale, de-emphasizing the significant clustering around $\Delta[O_2] = 0$ in favor of showing the few outliers. (c,f) Absolute $\Delta[O_2]$ values averaged over depth and time for 1° latitude by 1° longitude grid cells in the global ocean for (c) withheld observational data and (f) GFDL-ESM4 model output.

3.1.2 Test with GFDL-ESM4 output

As introduced in section 2.3, we refer to the four-dimensional field of $[O_2]_{est}$ values calculated by applying $ENS_{ESM4-Eval}$ algorithms to GFDL-ESM4 output as GOBAI-O$_2$-ESM4. $[O_2]_{est}$ values from GOBAI-O$_2$-ESM4 tracked closely with $[O_2]_{mod}$ and showed no significant systematic biases with $[O_2]$ or depth (Fig. 2d and 2e). Similar to the data-based test, variability in $\Delta[O_2]$ was greatest from just below the surface to about 500 meters. Average offsets were between −0.7 and 1.0 µmol kg^{-1} for the seven regions (with a global average of −0.1 µmol kg^{-1}) and RMSDs were between 3.3 and 9.0 µmol kg^{-1} for the seven basins (with a global average of 6.6 µmol kg^{-1}) (Table 2). The near-zero global average offset suggests that $[O_2]_{est}$ values from GOBAI-O$_2$-ESM4 matched well with values from GFDL-ESM4 output. The lowest RMSDs were found in the Southern Ocean and Arctic regions (Table 2; Fig. 2f), likely because these regions have significant amounts of available training data (Figure 1).
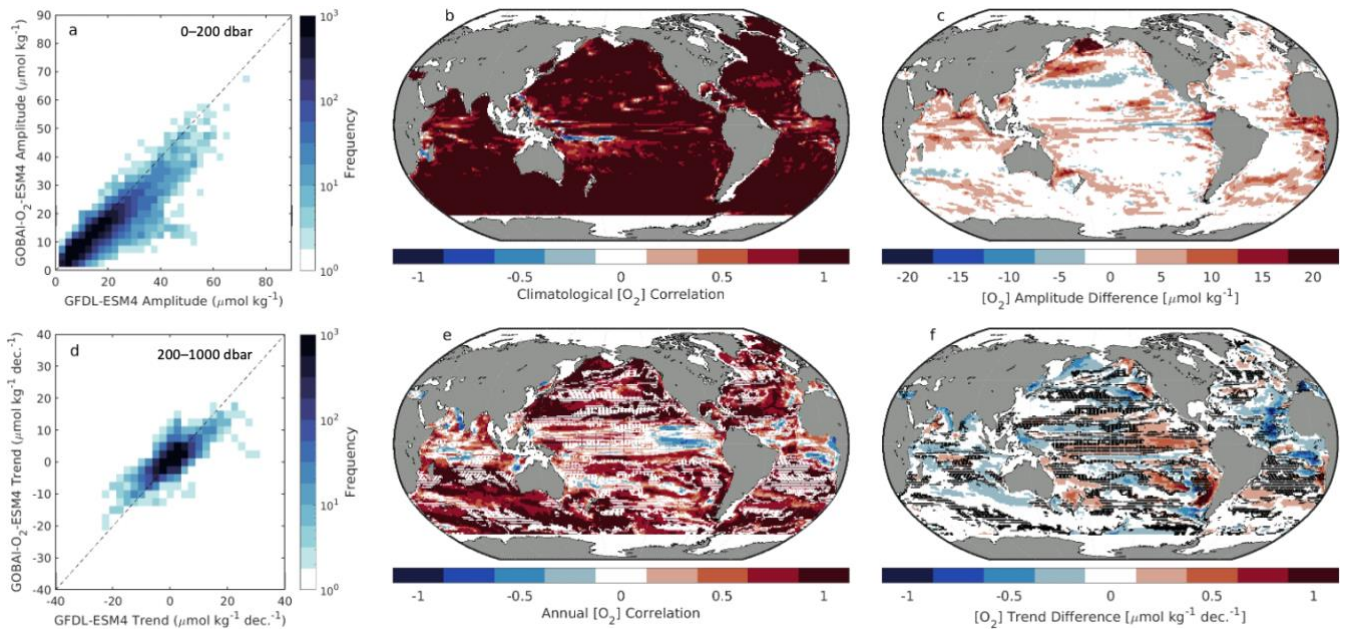
12

Figure 3. (a,d) Two-dimensional histograms showing grid cell level (a) climatological seasonal amplitudes in monthly mean [O$_2$] (weighted means according to the size of each depth interval) from 0 to 200 dbars and (d) trends in annual mean [O$_2$] from 200 to 1000 dbars between GFDL-ESM4 and GOBAI-O$_2$-ESM4. (b,e) Pearson's correlation coefficients between GFDL-ESM4 and GOBAI-O$_2$-ESM4 for (b) monthly mean [O$_2$] from 0 to 200 dbars, showing coherence between the surface seasonal cycles, and (e) annual mean [O$_2$] from 200 to 1000 dbars, showing coherence between the subsurface trends. (c,f) Absolute difference between GFDL-ESM4 and GOBAI-O$_2$-ESM4 for (c) climatological seasonal amplitudes in monthly mean [O$_2$] from 0 to 200 dbars and (f) trends in annual mean [O$_2$] from 200 to 1000 dbars. (e,f) Stippling indicates grid cells in which the GFDL-ESM4 trend is not significantly different from zero.

In addition to direct comparisons of [O$_2$] values, GOBAI-O$_2$-ESM4 effectively captured decadal scale and seasonal variability in [O$_2$] at the grid-cell level in the GFDL-ESM4 model environment (Fig. 3; Fig. A8–A10; Table 3). The average Pearson's correlation coefficient between gridded monthly mean [O$_2$] integrated from 0 to 200 dbars from GFDL-ESM4 output versus GOBAI-O$_2$-ESM4 was 0.92 ± 0.19 (Fig. 3b), and the seasonal amplitudes differed in magnitude (GFDL-ESM4 minus GOBAI-O$_2$-ESM4) by 1.9 ± 3.8 µmol kg^{-1} (Fig. 3c). The average Pearson's correlation coefficient between gridded annual mean [O$_2$] integrated from 200 to 1000 dbars from GFDL-ESM4 output versus GOBAI-O$_2$-ESM4 was 0.67 ± 0.36 (Fig. 3e), and the trends differed in magnitude (GFDL-ESM4 minus GOBAI-O$_2$-ESM4) by -0.3 ± 2.0 µmol kg^{-1} dec^{-1} (Fig. 3f).

When considered on the global scale, mean values, seasonal cycle amplitudes, long-term trends, and interannual variabilities in [O$_2$] matched well between GFDL-ESM4 output and GOBAI-O$_2$-ESM4 (Table 3). In almost every case, agreement was far better than it was when simply considering GFDL-ESM4 grid cells for which observations are available over this time period, with no spatiotemporal interpolation. For example, the trend in monthly mean [O$_2$] integrated from 0 to 2000 dbars was -0.38 µmol kg^{-1} dec^{-1} for GFDL-ESM4 output versus -0.31 µmol kg^{-1} dec^{-1} for GOBAI-O$_2$-ESM4 (Fig. A11). On the other hand,

13

grid cells where observations are available actually indicated an increase in monthly mean [O$_2$] integrated from 0 to 2000 dbars of 6.0 µmol kg^{-1} dec^{-1} over this time period when no spatiotemporal interpolation is applied.

375

Table 3. Statistics representing the mean values, seasonal cycle amplitudes, long-term trends, and interannual variabilities of [O$_2$] from the GFDL-ESM4 model, a reconstruction of [O$_2$] fields from GFDL-ESM4 using the approach of GOBAI-O$_2$ (GOBAI-O$_2$-ESM4), and subsampled grid cells from GFDL-ESM4 where and when real observations are available. Global weighted means (µ) of grid-cell level values are shown, along with differences (Δ) between the fully resolved GFDL-ESM4 means versus GOBAI-O$_2$-ESM4 and versus the subsampled GFDL-ESM4 grid cells.

Metric	Depth Interval (dbar)	GFDL-ESM4 µ	GOBAI-O$_2$-ESM4 µ	GOBAI-O$_2$-ESM4 Δ	Subsampled GFDL-ESM4 µ	Subsampled GFDL-ESM4 Δ
Mean [O$_2$] (µmol kg^{-1})	0−200	214.02	214.18	−0.17	230.21	−16.19
	200−1000	154.83	155.18	−0.35	173.62	−18.79
	0−2000	155.59	155.75	−0.16	169.58	−13.99
Seasonal Cycle Amplitude (µmol kg^{-1})	0−200	12.04	10.16	1.88	12.05	−0.01
	200−1000	3.37	2.11	1.27	5.94	−2.57
	0−2000	2.60	1.87	0.73	3.89	−1.29
Long−term Trend (µmol kg^{-1} dec.$^{-1}$)	0−200	−0.30	−0.26	−0.04	6.58	−6.88
	200−1000	−0.48	−0.23	−0.25	3.97	−4.46
	0−2000	−0.38	−0.18	−0.20	6.05	−6.43
Interannual Variability (µmol kg^{-1})	0−200	0.22	0.22	0.00	9.05	−8.83
	200−1000	0.29	0.18	0.11	10.59	−10.30
	0−2000	0.22	0.12	0.10	10.43	−10.21

Whether the internal variability in GFDL-ESM4 is truly representative of the ocean or is biased in one or more dimensions, the success of GOBAI-O$_2$-ESM4 in this evaluation exercise demonstrates an ability for the ML algorithms employed here to capture that variability with the current distribution of available [O$_2$] observations as training data. This bodes well for the ability of GOBAI-O$_2$, which is trained on actual observational data, to represent decadal scale and seasonal variability in global ocean oxygen in the real world. However, the GFDL-ESM4 output has undergone substantial spatial and temporal averaging and has no observational uncertainties, and thus the assessed skill can be thought of as an upper limit of the reconstruction skill achievable with the currently available observations.

390 The results of the exercise with GFDL-ESM4 model output are critical for evaluating the uncertainty of gridded oxygen values in GOBAI-O$_2$ (section 3.2.4). Further, the spatial distribution of Δ[O$_2$] (Fig. 2f) and the comparisons of reconstructed to modeled decadal trends and seasonal variability (Fig. 3b, 3c, 3e, 3f) can help inform our observing efforts (e.g., future cruise planning and BGC Argo float deployments). For example, large Δ[O$_2$] values in the eastern tropical Pacific and eastern tropical Atlantic, coupled with some negative correlations in annual mean [O$_2$] and differences in annual trends and seasonal amplitudes, suggest more observations will be required for GOBAI-O$_2$ (or likely any gap-filled [O$_2$] data product) to fully capture variability in that region.

3.2 GOBAI-O₂ product

3.2.1 Spatial oxygen distribution

The full GOBAI-O₂ product is available at https://doi.org/10.25921/z72m-yz67 (Sharp et al., 2023; last access: 19 Mar. 2023).

400   Vertical–meridional sections of oxygen (Figs. 4 and 5) show that surface oxygen concentrations are generally high, as these waters tend to be near equilibrium with the atmosphere. This is particularly true at high latitudes where cold, dense waters have a high capacity for dissolved oxygen. Southern Ocean surface waters, however, are generally undersaturated with respect to oxygen (Fig. A12), consistent with observations from previous studies that suggest this undersaturation is the result of O₂-depleted thermocline water upwelling into the mixed layer (Chierici et al., 2004; Reuer et al., 2007; Jonsson et al., 2013)

405   making the Southern Ocean on average an oxygen sink (Gruber et al., 2001; Bushinsky et al., 2017). This phenomenon can also be observed in the equatorial Pacific (Fig. A12). Undersaturation in high-latitude regions that are ice-covered during parts of the year can also be the result of limited air sea gas exchange when sea ice is present.
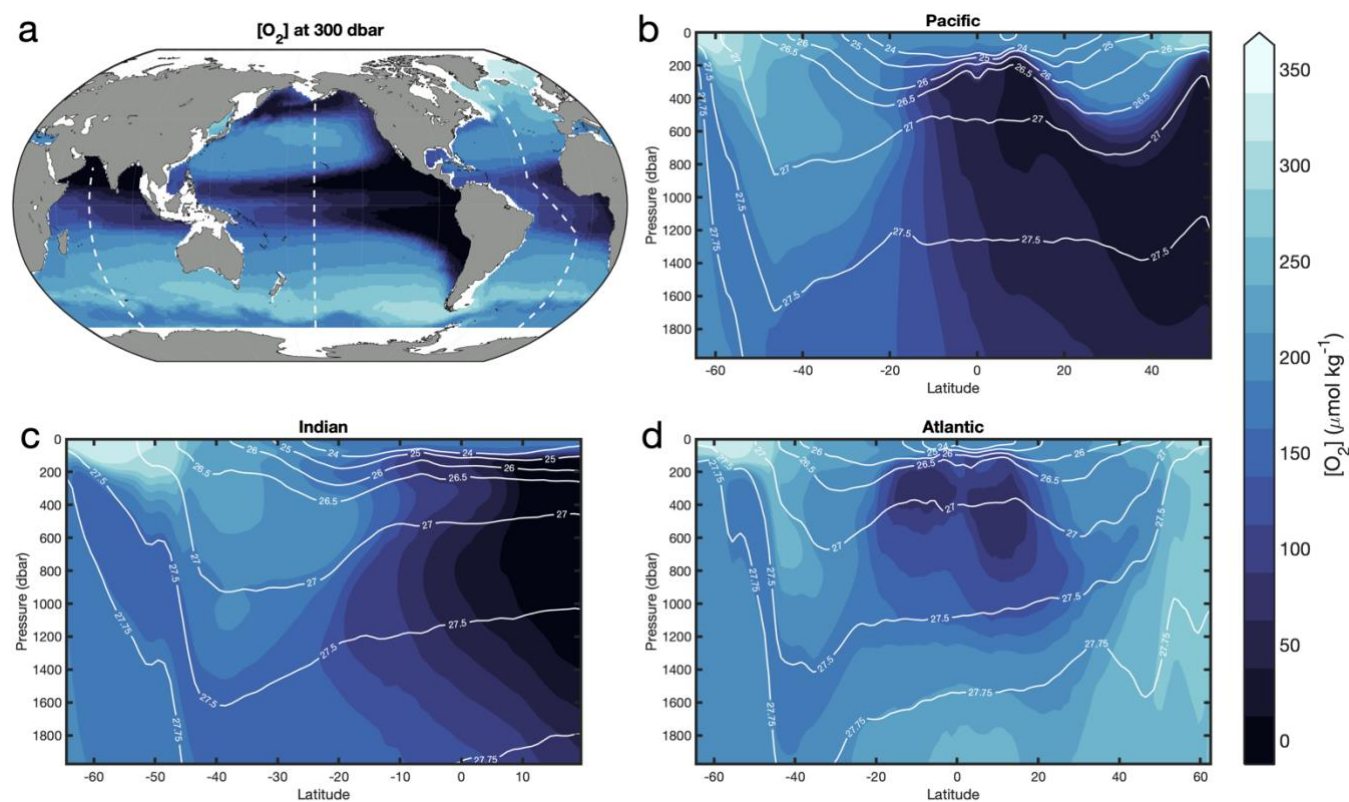
410   **Figure 4.** Long-term mean $[O_2]$ from GOBAI-O₂ at (a) 300 dbars and from the surface to 2000 dbars in the (b) Pacific, (c) Indian, and (d) Atlantic Oceans. White dashed lines in panel a show the locations of the sections in panels b–d. White contour lines in panels b–d are potential isopycnals (kg m^{-3}).
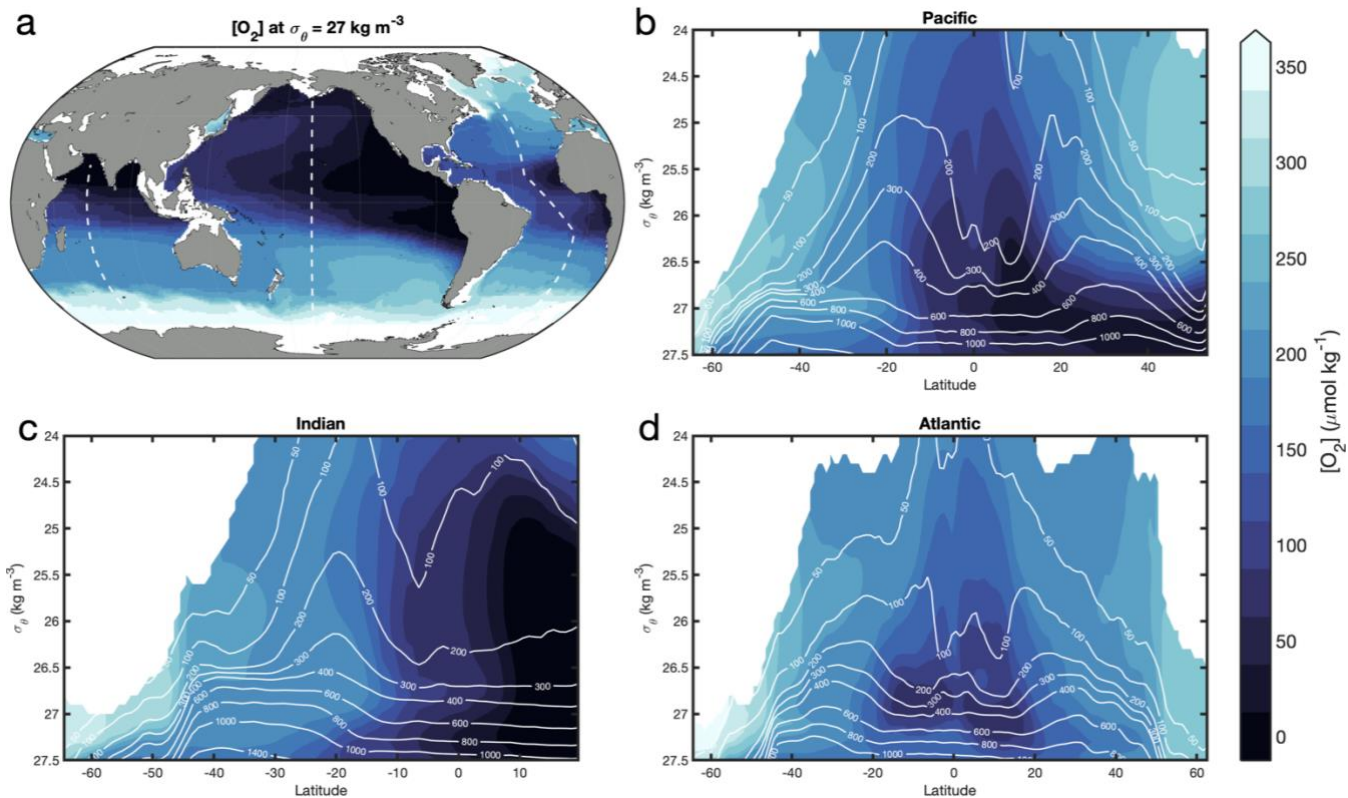
Figure 5. Long-term mean [O_2] from GOBAI-O_2 at (a) $\sigma_\theta = 27$ kg m^{-3} and from $\sigma_\theta = 24$ to 27.5 kg m^{-3} in the (b) Pacific, (c) Indian, and (d) Atlantic Oceans. White dashed lines in panel a show the locations of the sections in panels b–d. White contour lines in panels b–d are constant isobars (dbars).

Isobaric maps, isopycnal maps, and vertical–meridional sections with pressure and density vertical coordinates (Figs. 4 and 5) also reveal the [O_2] signatures of distinct subsurface water masses. In each basin, well-ventilated subtropical mode waters can be identified by relatively high [O_2] at mid-latitudes on the 300 dbar surface (Fig. 4a) and along dips in isopycnals plotted against pressure and latitude (Fig. 4b–d) or along sloping isobars plotted against density and latitude (Fig. 5b–d) within the upper ~500 dbars. Beneath the southern mode waters in each basin, Antarctic Intermediate Water that originates in the Southern Ocean with a relatively high [O_2] signal is prevalent. Beneath northern mode waters in the Pacific and Indian basins, respectively, relatively old and oxygen-poor North Pacific Intermediate Water (NPIW) and Red Sea Overflow Water (RSOW) can be observed (Talley et al., 2011). Beneath northern mode waters in the Atlantic, intermediate waters are younger and more highly oxygenated. Near the equator, subsurface oxygen minima are visible in each basin; this is a result of organic matter export from high production in the surface ocean that fuels strong subsurface respiration and relatively poor ventilation (old waters) in this region. Finally, the signatures of higher oxygen deep or bottom waters can be observed near the bottom or at high latitudes in each vertical–meridional section.

16

Oxygen concentrations at 300 dbars (Fig. 4a) are highest in the North Atlantic and Southern Oceans — where highly oxygenated, newly formed deep and intermediate waters are formed — and lowest in the North and Equatorial Pacific Ocean and the North Indian Ocean — where the oxygen content of subsurface waters has been greatly reduced by heterotrophic respiration over time. The same can be said for $[O_2]$ on the 27.0 kg m^{-3} σ_θ surface (Fig. 5a). Oxygen concentrations are extremely low in the deep, high-density North Pacific Ocean (Figs. 4b and 5b) and North Indian Ocean (Figs. 4c and 5c) due to the accumulated effects of oxygen-depleting respiration over the long lifespans of those water masses (i.e., long time since gas exchange with the atmosphere).
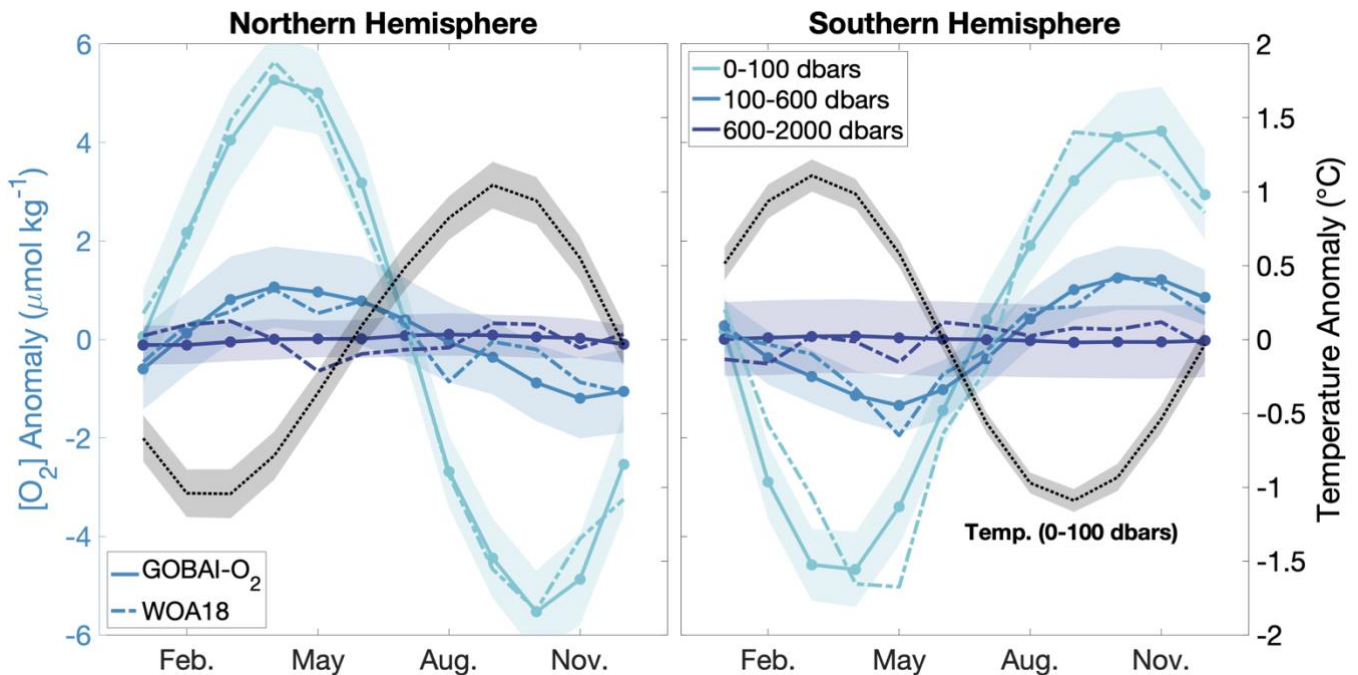

Figure 6. Climatological seasonal cycles of $[O_2]$ anomalies (monthly $[O_2]$ minus long-term mean $[O_2]$) integrated globally over three pressure intervals: 0–100, 100–600, and 600–2000 dbars. The black dotted line shows climatological temperature anomaly integrated globally over the 0–100 dbar interval. Shading indicates the standard deviation of the climatological seasonal cycle from 2004 to 2022. The dashed lines show climatological seasonal cycles of $[O_2]$ anomalies from WOA18 over similar depth intervals to GOBAI-O2: 0–100, 100–600, and 600–1500 meters.

3.2.2 Climatological seasonal oxygen cycles

Seasonal cycles in $[O_2]$ reflect a balance among physical and biological processes (Wang et al., 2022). Climatological hemispheric mean $[O_2]$ integrated over three pressure intervals from GOBAI-O$_2$ (Fig. 6) reveals that the magnitude of the $[O_2]$ seasonal cycle is greatest near the surface and decreases with depth. The amplitude of the $[O_2]$ seasonal cycle in a near-surface interval (0–100 dbars) is about 10.8 µmol kg^{-1} in the Northern Hemisphere and 8.9 µmol kg^{-1} in the Southern Hemisphere.

17

Maximum [O_2] in this depth interval (April/May in the Northern Hemisphere and October/November in the Southern Hemisphere) lags about two months behind the temperature minimum, suggesting an interaction between a thermally driven increase in oxygen solubility and biologically driven oxygen production. Minimum [O_2] in the near-surface interval (October in the Northern Hemisphere and March/April in the Southern Hemisphere) is more coincident with the temperature maximum, indicating primary control by a thermally driven decrease in oxygen solubility. The amplitude of the [O_2] seasonal cycle is about 2.3 µmol kg^{-1} in the Northern Hemisphere and 2.6 µmol kg^{-1} in the Southern Hemisphere in an intermediate interval (100–600 dbars), and about 0.2 µmol kg^{-1} in the Northern Hemisphere and 0.1 µmol kg^{-1} in the Southern Hemisphere in a deep interval (600–2000 dbars). The timing of maximum [O_2] values is similar between the near-surface interval and intermediate interval in both hemispheres, indicating the well-mixed nature of the ocean in winter and early spring when [O_2] is high. On the other hand, minimum [O_2] in the intermediate interval lags behind that in the near-surface interval in both hemispheres, possibly reflecting higher stratification in the upper ocean when temperatures are warmer and/or the remineralization of sinking organic matter after summer production. Further analysis of climatological [O_2] cycles from GOBAI-O_2 can provide insight into the physical and biological factors that control surface and subsurface oxygen on regional and global scales.

3.2.3 Interannual oxygen variability

Deoxygenation is evident in GOBAI-O_2 over the past two decades, coincident with ocean warming (Fig. 7; Table B5). The spatially weighted rate of deoxygenation in the upper two kilometers globally (along with a 90% confidence interval) is -1.06 ± 0.20 µmol kg^{-1} dec.$^{-1}$ (-0.71 ± 0.13 % dec.$^{-1}$). The rate of deoxygenation in GOBAI-O_2 varies over depth, with a near-surface interval (0–100 dbars) displaying a trend in [O_2] of -1.00 ± 0.51 µmol kg^{-1} dec.$^{-1}$ (-0.45 ± 0.23 % dec.$^{-1}$), an intermediate interval (100–600 dbars) -1.09 ± 0.34 µmol kg^{-1} dec.$^{-1}$ (-0.68 ± 0.21 % dec.$^{-1}$), and a deep interval (600–2000 dbars) -1.06 ± 0.36 µmol kg^{-1} dec.$^{-1}$ (-0.75 ± 0.26 % dec.$^{-1}$). Interannual variability is greatest in the near-surface interval: when the multi-year trends and seasonal cycles are removed, the standard deviation of annual global mean [O_2] anomalies is 0.53 µmol kg^{-1} in the near-surface interval compared to 0.21 µmol kg^{-1} in the intermediate interval and 0.11 µmol kg^{-1} in the deep interval. Trends and uncertainties were determined by fitting linear least squares models to spatially weighted monthly mean [O_2] and monthly oxygen inventories integrated over the specified depth intervals, with uncertainties in monthly values determined by comparing GOBAI-O_2-ESM4 to GFDL-ESM4; more information on this is provided in Appendix E.

Ocean warming has a direct effect on oxygen concentrations by lowering the solubility of O_2 in ocean water (Garcia and Gordon, 1992). Solubility changes explain about 62% of deoxygenation in the near-surface ocean interval (0–100 dbars), 26% in the intermediate ocean interval (100–600 dbars), and 15% in the deep ocean interval (600–2000 dbars) (Fig. 7c and 7f). The remaining deoxygenation must then be caused by indirect consequences of ocean warming (such as increased ocean stratification hence decreased subsurface ventilation) or other processes, including changes to oxygen utilization and ocean ventilation variability (Oschlies et al., 2018), the magnitudes of which this analysis does not attempt to deconvolve. The RG09

18

485 temperature and salinity fields are constructed such that they relax toward the climatological means during periods of low data density. For this reason, temperature is biased somewhat high (Figs. 7b and 7e) and therefore O_2 solubility biased somewhat low (Figs. 7c and 7f) toward the beginning of the time series when fewer observations are available. This artifact may influence GOBAI-O_2 (Figs. 7a and 7d) since it was constructed using the RG09 temperature and salinity fields; however, its influence is partially mitigated because temporal information included in the training and application of the GOBAI-O_2 algorithms allows

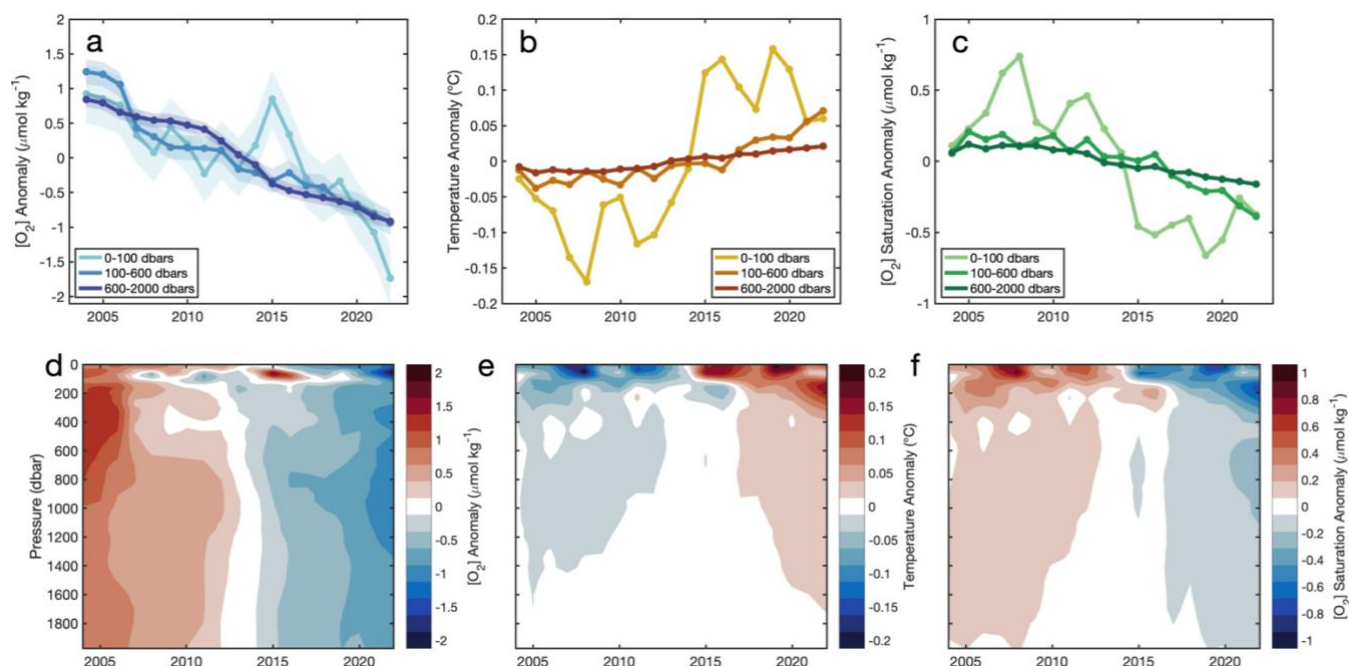490 for the trend inherent to the underlying oxygen data to be retained.

Figure 7. (a,b,c) Annual mean (a) [O_2] anomalies from GOBAI-O_2, (b) temperature anomalies from RG09, and (c) [O_2]$_{sat.}$ anomalies calculated from RG09 temperature and salinity fields, each integrated globally over three pressure intervals: 0–100,
495 100–600, and 600–2000 dbars. (a) Shading represents uncertainty determined as the average difference between mean [O_2] from GOBAI-O_2-ESM4 versus GFDL-ESM4 in each interval. (d,e,f) Hovmöller diagrams showing annual mean (d) [O_2] anomalies from GOBAI-O_2, (e) temperature anomalies from RG09, and (f) [O_2]$_{sat.}$ anomalies calculated from RG09 temperature and salinity fields, each over depth in decibars from 2004 to 2022. Anomalies in each parameter are calculated as annual mean values minus the long-term mean either (a–c) integrated over a depth interval or (d–f) on a given depth level.

500

GOBAI-O_2 trends can be viewed in the context of other recent analyses that explore long term changes in ocean oxygen. From the surface to 1000 dbars, the GOBAI-O_2 trend of -0.72 ± 0.13 % dec.$^{-1}$ from 2004–2022 is comparable to that assessed by Bindoff et al. (2019) of -0.48 ± 0.35 % dec.$^{-1}$ from 1970–2010 (surface to 1000 meters), which takes into account estimates from Helm et al. (2011) (-0.44 ± 0.14 % dec.$^{-1}$), Schmidtko et al. (2017) (-0.34 ± 0.35 % dec.$^{-1}$), and Ito et al. (2017) (-0.68
505 ± 0.33 % dec.$^{-1}$). In the surface interval (0–100 dbars), the GOBAI-O_2 trend of -0.45 ± 0.23 % dec.$^{-1}$ is larger than, though within uncertainties of, the Bindoff et al. (2019) assessment of -0.28 ± 0.24 % dec.$^{-1}$; in the intermediate interval (100–600

dbars) the GOBAI-O_2 trend of -0.68 ± 0.21 % dec.$^{-1}$ is also larger than, though again comparable to, the Bindoff et al. (2019) assessment of -0.52 ± 0.36 % dec.$^{-1}$. While these comparisons represent different periods of time such that one should not expect perfect agreement, we find the consistency encouraging. The somewhat more negative GOBAI-O_2 trends compared to previous estimates also suggest a possible acceleration on ocean deoxygenation over the last decade or so, which would be consistent with expectations (Kwiatkowski et al., 2020). Further, close agreement between GOBAI-O_2 and other observation-based studies provides additional support for the notion that current ESMs, which exhibit weaker deoxygenation trends, may not fully capture the sensitivities of physical and biological processes leading to deoxygenation (Oschlies et al., 2017; 2018; Stramma and Schmidtko, 2021). This comparison not only places the GOBAI-O_2 trends in a longer term context but suggests that the enhanced observations and analysis result in a reduced trend uncertainty despite the comparatively-shorter 19-year record (± 0.13 % dec.$^{-1}$) versus the longer but more sparse 40-year record available to Bindoff et al. (± 0.35 % dec.$^{-1}$; 2019).

Finally, the trends presented here represent both natural and potentially anthropogenic variability over the interval between 2004 and 2022, as well as uncertainties in the algorithm predictions (see section 3.2.4). As such, these trends should not be interpreted to be driven exclusively by ocean warming and other associated impacts of anthropogenic climate change. This is especially true of the regional trends. The period of time examined is relatively short and the domain is not inclusive of the entire global ocean. Accordingly, decadal-scale variability in ocean ventilation, interior circulation, and biological oxygen utilization may exert significant influence over these trends.

3.2.4 Uncertainty

GOBAI-O_2 uncertainty fields, which were estimated as described in section 2.5, can be used to assess confidence in multi-year trends and seasonal cycles of [O_2], both on a global and regional scale. Time-averaged uncertainty fields at 150 dbar (Fig. 8) suggest that the largest contributor overall is the algorithm uncertainty. Algorithm uncertainty is also the most geographically variable. Averaged globally over space and time, $u([O_2])_{meas.}$ was equal to 2.3 µmol kg^{-1} (2.8 µmol kg^{-1} on the 150 dbar level), $u([O_2])_{grid.}$ was equal to 2.9 µmol kg^{-1} (5.3 µmol kg^{-1} on the 150 dbar level), and $u([O_2])_{alg.}$ was equal to 3.8 µmol kg^{-1} (6.2 µmol kg^{-1} on the 150 dbar level). Combined, $u([O_2])_{tot.}$ (Eq. 1) was equal to 6.0 µmol kg^{-1} (9.6 µmol kg^{-1} on the 150 dbar level), which can be compared to the global average RMSD of 8.6 µmol kg^{-1} determined independently by withholding data from algorithm training (Table 2, Fig 2a-2c).

Measurement uncertainty provides an estimate of confidence in an [O_2] value assigned to a water sample by direct measurement; gridding uncertainty provides an estimate of confidence that the [O_2] value provided for a four-dimensional grid cell might represent [O_2] at any point in time and space within that grid cell; and algorithm uncertainty provides an estimate of confidence that the predicted [O_2] value for a given grid cell is appropriate as the average value for that grid cell. Algorithm uncertainty in particular depends upon the distribution of data available to train the ML algorithms and the ability of the trained algorithms to represent underlying variability in the system. On the depth level shown in Fig 8. (150 dbar), the underlying

20

540   variability is relatively high in [O_2] minimum zones (e.g., near the equator and on the eastern boundaries of ocean basins), hence the elevated algorithm (and total) uncertainties in those regions. Here, algorithm uncertainty was assessed via the exercise with synthetic data from GFDL-ESM4 (see sections 2.3 and 3.1.2).
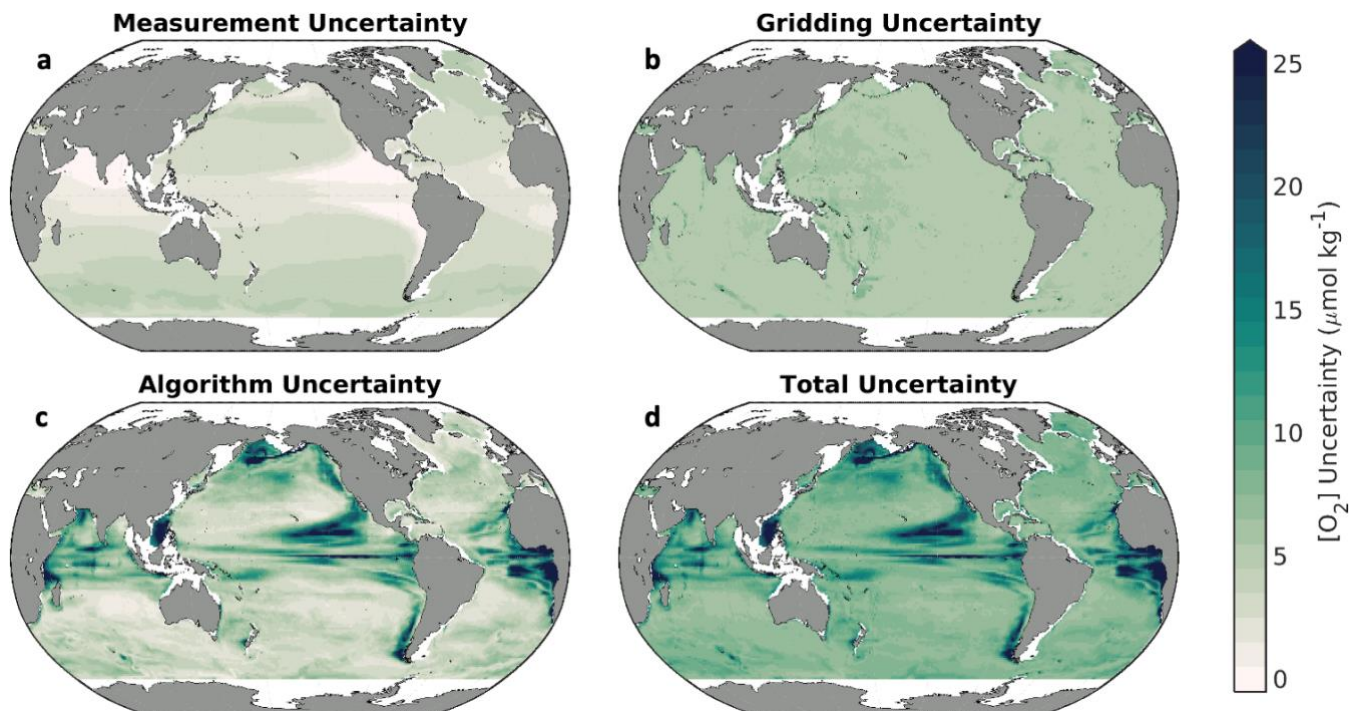
545   **Figure 8.** Long-term means of the uncertainty contributors to GOBAI-O_2 at 150 dbar, including (a) measurement uncertainty, (b) gridding uncertainty, (c) algorithm uncertainty, and (d) total uncertainty.

Algorithm uncertainty should in general decrease as the spatiotemporal coverage of available training data increases. Regionally, algorithm uncertainty depends upon the degree to which the underlying variability of the system is captured by
550   the available training observations and the ability of the ML algorithms to reconstruct that variability from concurrent measurements of other seawater properties. The fact that algorithm uncertainty is the largest uncertainty contributor in GOBAI-O_2 suggests that limitations in the ML algorithms used to fill spatiotemporal gaps in [O_2] outweigh limitations related to measurement quality and averaging data to four-dimensional bins. Comparing the Δ[O_2] map in Fig. 2f or the algorithm uncertainty map in Fig. 8c to the data distribution map in Fig. 1 or Fig. A1 suggests that sparse sampling is primarily to blame
555   for these limitations: high uncertainties tend to occur where observations are limited. Detailed analysis of GFDL-ESM4 water mass characteristics in the California Current System has also revealed that high uncertainties occur where water masses with similar physical characteristics but different oxygen signatures mix, underscoring that the measurement of additional biogeochemical parameters can supplement the physical/spatiotemporal-based [O_2] estimates presented here. Overall, the

dominance of algorithm uncertainty is consistent with uncertainty analysis conducted for gap-filling methods applied to other ocean biogeochemical variables (e.g., Landschützer et al., 2014; Gregor and Gruber, 2020). For this reason, continued expansion of oxygen observations in undersampled regions will be critical to reduce uncertainty in our gap filling, and ultimately our understanding, of global subsurface oxygen distributions and variability.
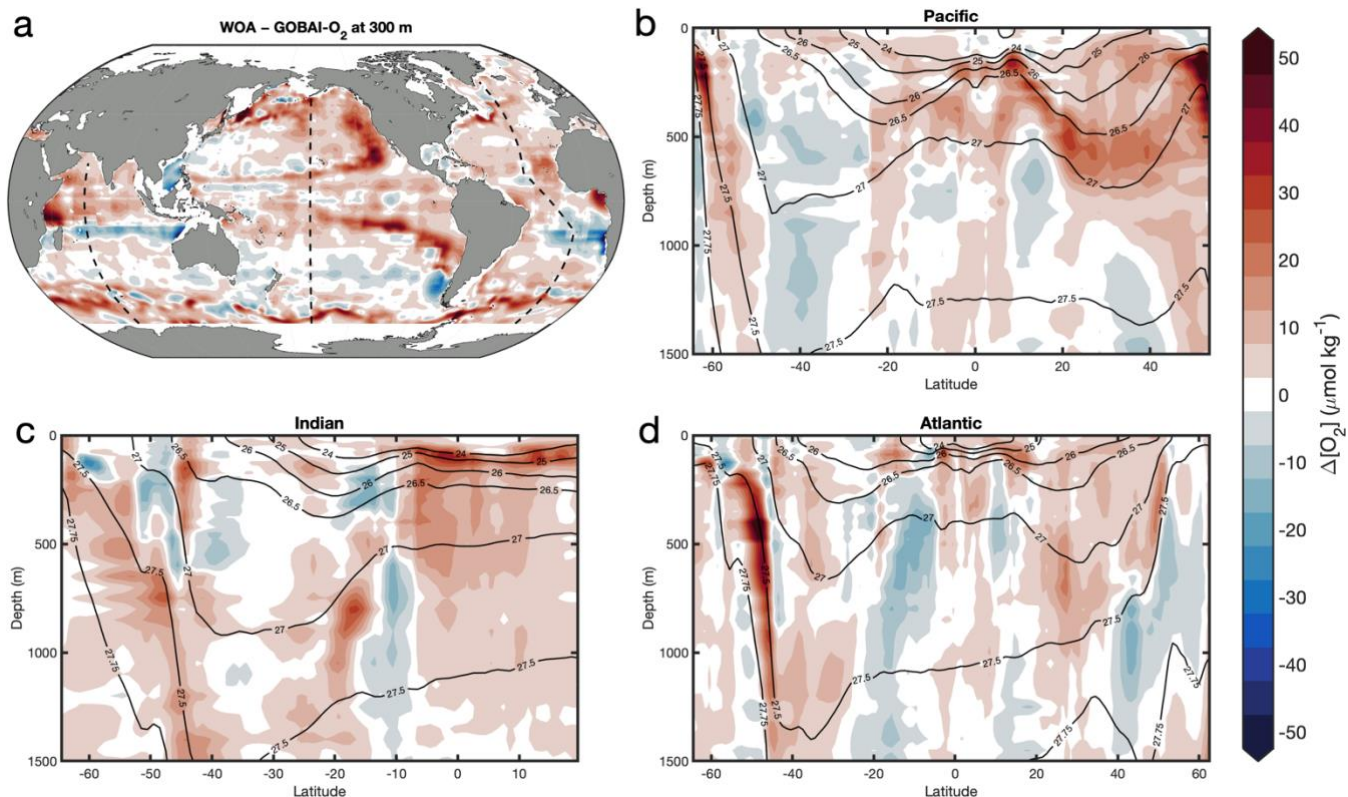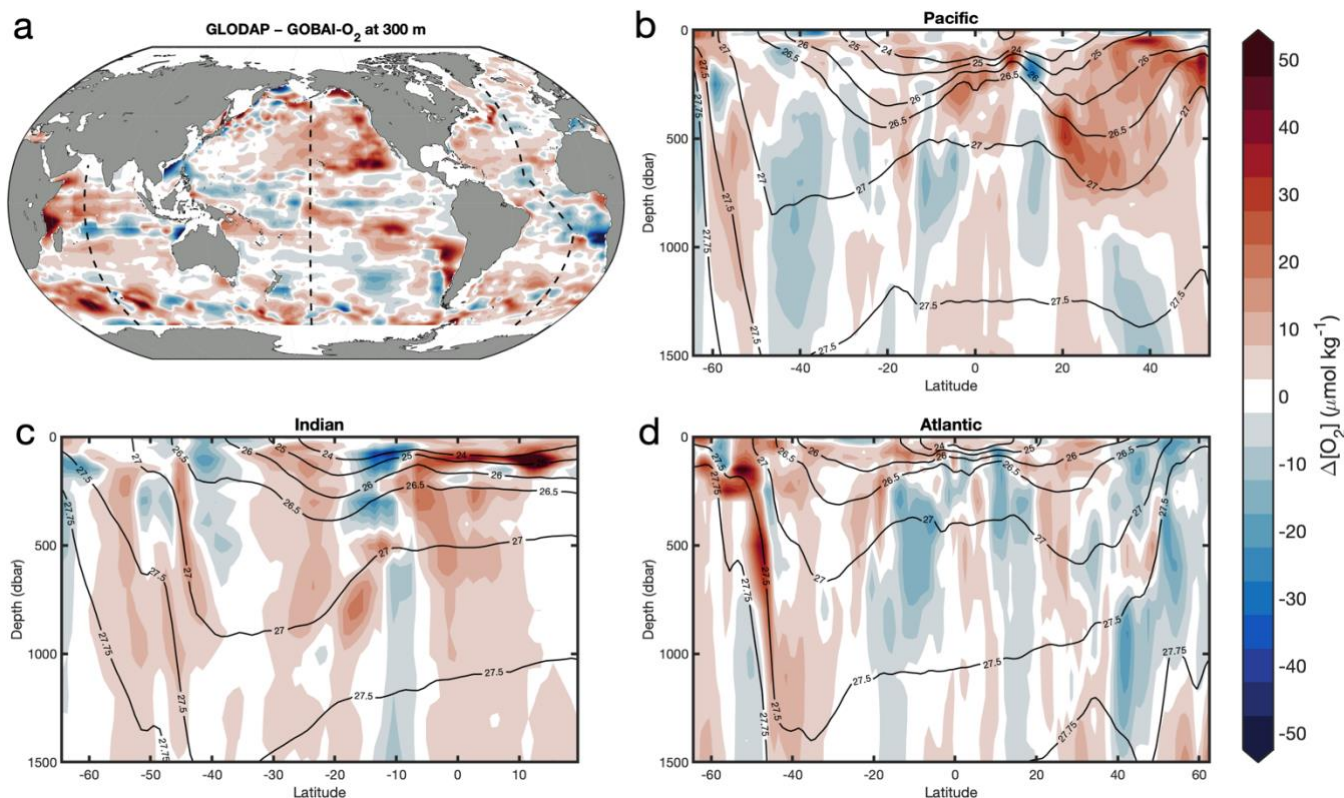

Figure 9. The difference between climatological mean [O_2] from WOA18 and long-term mean [O_2] from GOBAI-O_2 (Δ[O_2] = [O_2]$_{WOA}$ − [O_2]$_{GOBAI}$) at (a) 300 meters and from the surface to 1500 dbars in the (b) Pacific, (c) Indian, and (d) Atlantic Oceans.

Global mean depth profiles of uncertainty contributors (Fig. A14) emphasize the general attenuation of uncertainty away from the surface, with subsurface maxima of algorithm uncertainty and total uncertainty at 200 dbars. These maxima correspond to depths at which vertical gradients in [O_2] are relatively high (see Fig. 4). Here, small variations in the depths of density surfaces can influence [O_2] on a given depth level; this variability is challenging to capture, even with potential density as a predictor variable in the ML models (see Table 1).

3.2.5 Comparison to other gridded products

575 The long-term mean field of [O_2] from GOBAI-O_2 was compared to the corresponding mean field of [O_2] from the WOA18 monthly climatology (Fig. 9) and climatological field of [O_2] from the GLODAPv2.2016 mapped product (Fig. 10). On average, GOBAI-O_2 oxygen concentration is 9.8 µmol kg^{-1} lower than WOA18 and 1.1 µmol kg^{-1} lower than GLODAP. This can be partly explained by the fact that GOBAI-O_2 is centered on the year 2012, whereas WOA18 takes into account [O_2] observations dating back to 1965, observations in GLODAPv2.2016 are centered around 2002 (Lauvset et al., 2016), and

580 global deoxygenation has occurred in recent decades (Bindoff et al., 2019). Spatially, the largest differences occur within and especially near the boundaries of oxygen minimum zones (eastern tropical Pacific, eastern Atlantic coastal zones, and northern Indian), along $\sigma \approx 27.5$ kg m^{-3} in the Southern Ocean, and along $\sigma \approx 26.75$ kg m^{-3} in the North Pacific. It is difficult to determine whether these differences are functions of data availability (ship data for WOA18 and GLODAP versus ship and float data for GOBAI-O_2), representative time period, or mapping method (objective interpolation for WOA18 and GLODAP versus

585 machine learning algorithms for GOBAI-O_2). A future intercomparison exercise between mapping methods using an identical starting dataset could be helpful in diagnosing these differences among gridded products.

Figure 10. The difference between 2002-centered mean [O_2] from the GLODAPv2.2016 mapped product and long-term mean
590 [O_2] from GOBAI-O_2 (Δ[O_2] = [O_2]$_{GLODAP}$ − [O_2]$_{GOBAI}$) at (a) 300 meters and from the surface to 1500 dbars in the (b) Pacific, (c) Indian, and (d) Atlantic Oceans.

3.2.6 Comparison to synoptic in situ measurements

GOBAI-O₂ was compared to direct observations from repeat hydrography cruises, including meridional transects across the
Atlantic (A16 in 2013 and A20 in 2021), Pacific (P16 in 2005), and Indian (I08 and I09 in 2016) Oceans, as well as a zonal
transect across the Pacific Ocean (P02 in 2012). This exercise assessed how well monthly [O₂] estimates from GOBAI-O₂
were able to represent high-quality [O₂] measurements at distinct points in time and space. Due to fundamental differences
between gridded estimates and point observations, we don't expect every matchup to be perfect. However, we would hope to
see general coherence in mean values across large-scale ocean sections and to see a pattern of differences that make sense
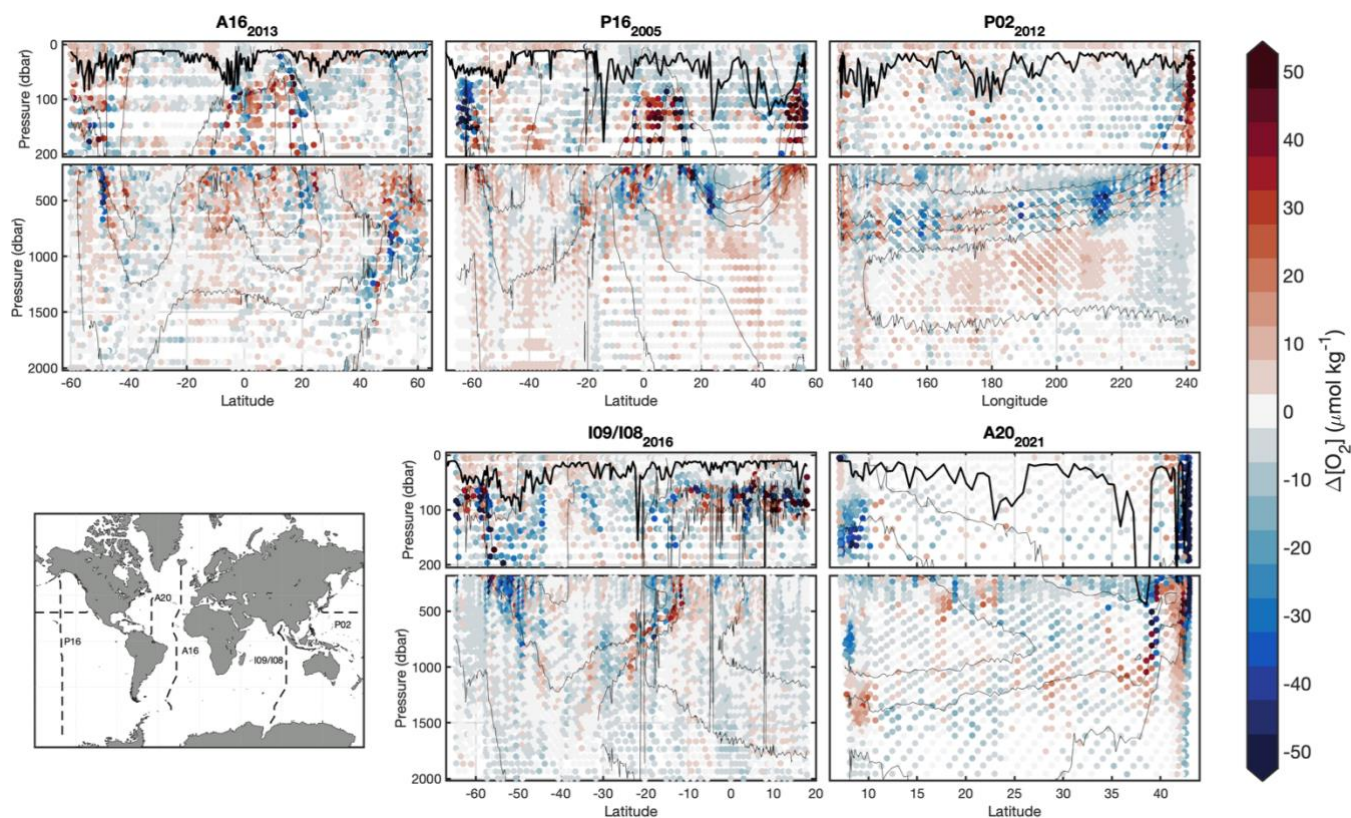given our *a priori* expectations.

Figure 11. Section plots displaying comparisons between discrete observations of [O₂] from repeat hydrography cruises and
[O₂] extracted from corresponding grid cells in GOBAI-O₂. Thick lines in each panel represent mixed layer depth calculated
as the depth at which potential density anomaly increased to 0.03 kg m⁻³ greater than potential density anomaly at 10 dbars.
Thin lines are contours representing increments of 50 μmol kg⁻¹ in [O₂].

For the cruise datasets examined, GOBAI-O₂ estimates matched fairly well with discrete measurements in the mixed layer and
below ~1000 dbars (Fig. 11). In intermediate depths, however, large differences occasionally occur. These large differences

610 tended to cluster around areas with strong vertical gradients in [O_2] (thin contours in Fig. 11 represent increments of 50 μmol in [O_2]). Comparison of Fig. 11 to Fig. A15 gives confidence to our uncertainty evaluation: larger differences between discrete measurements and GOBAI-O_2 occur where $u([O_2])_{tot.}$ is large. Median biases, mean biases, and RMSDs between direct observations and GOBAI-O_2 are given in Table B6.

4 Conclusions

615 GOBAI-O_2 is a major step toward the fulfilment of the primary goal set out by Gruber et al. (2010): "to determine, on a global-scale, seasonal to decadal time-scale variations in dissolved oxygen concentrations throughout the upper ocean". Quantifying these variations is important for documenting ocean deoxygenation, determining global net primary productivity and carbon export, and facilitating studies of the oceanic uptake of anthropogenic CO_2. In addition, insights into ocean biogeochemical dynamics, when observations are unavailable, often come from ocean models, and GOBAI-O_2 can bring value to modelling 620 studies by providing fields of [O_2] to be used for boundary conditions and model initialization. GOBAI-O_2 can also be useful as a dynamic reference check in data-sparse regions for new, sensor-based [O_2] measurements that would otherwise be compared to a static monthly climatology like WOA18. This all being said, the uncertainty analysis conducted here confirms that GOBAI-O_2 remains limited, primarily by sparse sampling. The most consequential action to improve GOBAI-O_2 fields over the next decade will be the continued deployment of Argo floats with oxygen optodes — emphasizing the importance of 625 bolstering the biogeochemical Argo array and expanding the international OneArgo network into high latitudes, the deep ocean, and marginal seas (Roemmich et al., 2019; 2021; Schofield et al., 2022) — and the continued collection of discrete dissolved oxygen observations, primarily through the international GO-SHIP program, both for use in the mapping and for calibration/validation of the Argo oxygen data..

630 Besides the collection of more observations, additional actions can be taken to improve GOBAI-O_2 fields. For one, more predictor variables and ML algorithms can be tested. Different processes dominate [O_2] variability in different regions (Keeling et al., 2010; Oschlies et al., 2018; Garcia-Soto et al., 2021), and certain predictor variables will be better suited for capturing these processes. Also, ML algorithms adapt to data sparseness and modes of variability in different ways (Ritter et al., 2017; Gregor et al., 2019), so estimates in a given region that are worse using one algorithm may be better using another. Therefore, 635 regionally-tuned predictors and more diverse ensembles of ML algorithms should lead to increased confidence in estimates of ocean interior [O_2].

Another action that could result in improved fidelity of GOBAI-O_2 fields is the use of predictor variable fields with higher spatial and temporal resolution across sharp biogeochemical gradients. Ocean profiles of temperature and salinity tend to be 640 relatively smooth, so a depth resolution on the order of tens of meters in the upper ocean increasing to hundreds of meters at depth is sufficient for gridded products. Biogeochemical parameters like oxygen, on the other hand, tend to be characterized

by profiles with sharp gradients and with distinct minima and maxima in the water column (Sarmiento and Gruber, 2006). These minima and maxima can occur very near the surface or hundreds of meters below it. For this reason, comparisons of GOBAI-O_2 to direct measurements of [O_2] can be uniquely problematic in the ~100–1000 dbar range when sharp gradients are present (Fig. 11). Biogeochemical gradients over horizontal space and time can also be sharp, especially in highly dynamic coastal zones and in the surface ocean where the residence time of oxygen is often less than a month (Luz and Barkan, 2000). Recent work from Lyman and Johnson (2023) uses Argo observations coupled with machine learning to provide well-resolved (7-day × ¼° grid) ocean heat content maps, and continued development toward maps of temperature and salinity could be helpful for overcoming the issue of resolving sharp biogeochemical gradients. Alternatively, [O_2] estimates could be made using temperature and salinity observations at their original resolution, then mapped onto four-dimensional grids that are uniquely suited in their spatial resolution for biogeochemical parameters. A necessary consideration of the latter option would be computing resources: applying complex ML algorithms to temperature and salinity measurements from Argo floats at their original resolution may prove to be impractical.

Finally, observations from additional platforms could be incorporated into approaches like this one to map [O_2] in the global ocean. Ocean gliders and moored profilers have long been equipped with oxygen optodes. These platforms collect data at unique spatiotemporal scales and could add predictive information for [O_2] that is not provided by Argo float observations or discrete shipboard measurements. To facilitate the incorporation of new data streams into the development of gridded data products, accessible databases should be created and maintained (Testor et al., 2019; Grégoire et al., 2021).

The method used to develop GOBAI-O_2 can be applied in a similar way to other ocean chemical parameters. In addition to dissolved oxygen, the BGC Argo program has deployed floats with sensors for measuring dissolved nitrate, pH, chlorophyll-a, particle backscatter, and downwelling irradiance. Machine learning methods have been used to develop four-dimensional fields of optical properties, i.e. chlorophyll-a and particle backscatter (Sauzède et al., 2015; 2016), and continued refinement of those fields is ongoing (Sauzède et al., 2021). Chemical properties, i.e. nitrate and pH, that exhibit distributions more similar to [O_2] are good candidates for adoption into the GOBAI mapping approach. Together with property estimation algorithms for TA (Bittig et al., 2018b; Carter et al., 2021), a mapped ocean interior pH product could be used to resolve the entire ocean carbonate system in four dimensions in near real time.

Ultimately, global changes to the amount of dissolved oxygen in ocean waters will have profound effects on the metabolism of marine organisms (Pörtner and Farrell, 2008; Sampaio et al., 2021) and the cycling of biogeochemically important elements (Gruber, 2004; Berman-Frank et al., 2008). Whereas ocean models agree that the ocean's oxygen inventory has been declining and will continue to decline, disagreement remains as to regional patterns of this deoxygenation. Direct observations are critical for the confirmation or contradiction of model trends. With this work we have turned to autonomous and discrete observations, with the assistance of machine learning algorithms, to bridge the model–observational gap. We produce and analyze a multi-

year gridded product of ocean dissolved oxygen called GOBAI-O_2, independently confirming a phenomenon that has been demonstrated previously: the ocean is losing dissolved oxygen at a rapid rate (0.71 ± 0.13 % dec.$^{-1}$ in the upper two kilometers according to GOBAI-O_2). In addition, we provide this valuable observation-based product for community use. GOBAI-O_2 can be turned to as a reference for [O_2] observations and model boundary conditions, compared to new and existing observational and model-based reconstructions of ocean deoxygenation, and used for critical analyses of seasonal to decadal and regional to global oxygen variability.

680

5 Appendices

Appendix A. Supplemental Figures
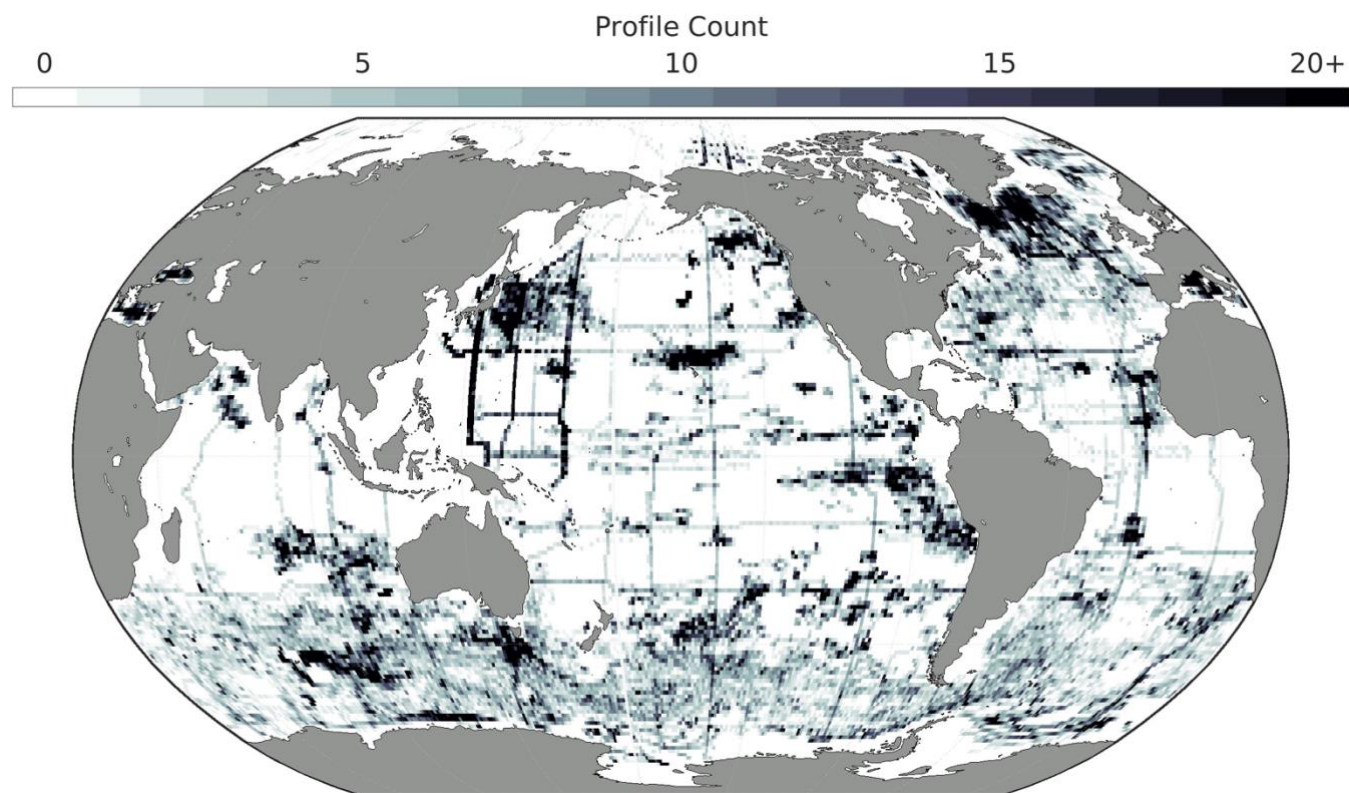
Figure A1. The number of profiles (either ship-based or Argo float-based) from the combined dataset used to train machine learning algorithms to produce GOBAI-O_2 that are contained within each $1° \times 1°$ box in the global ocean.
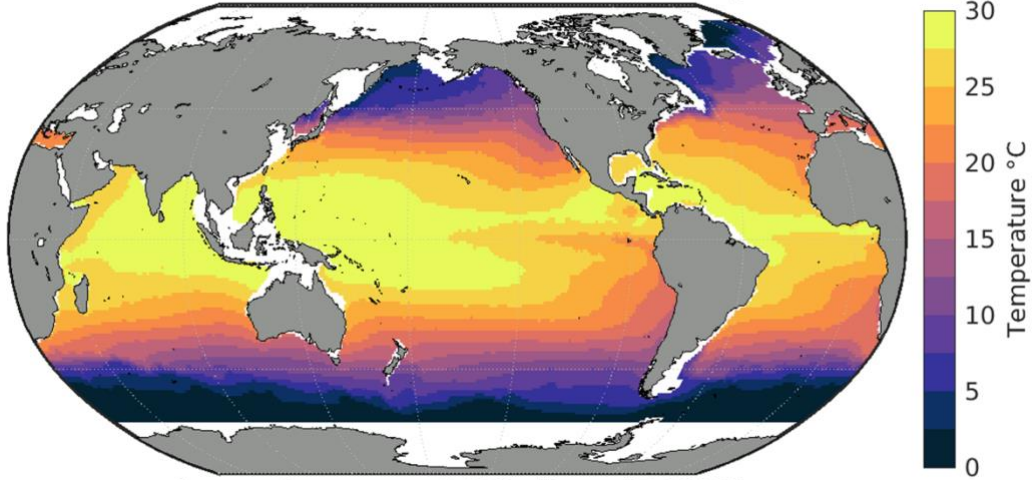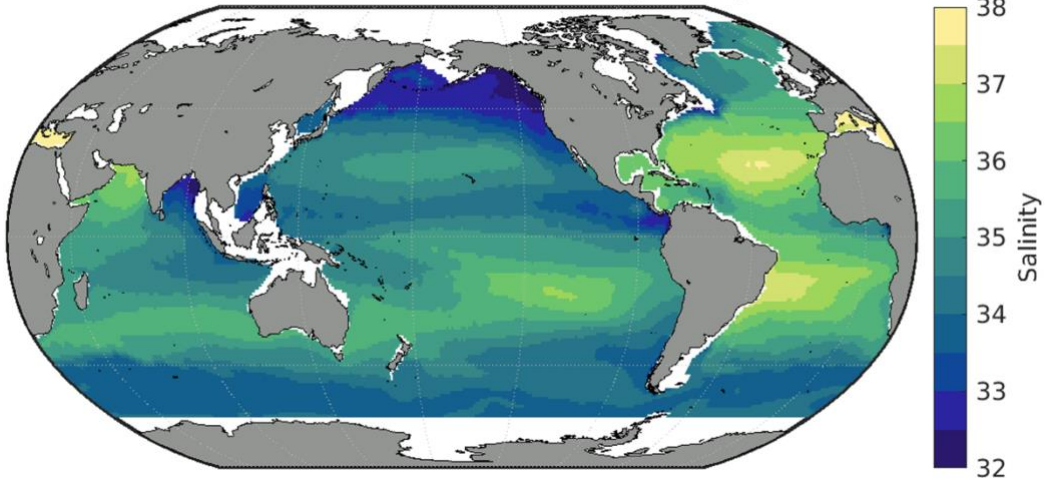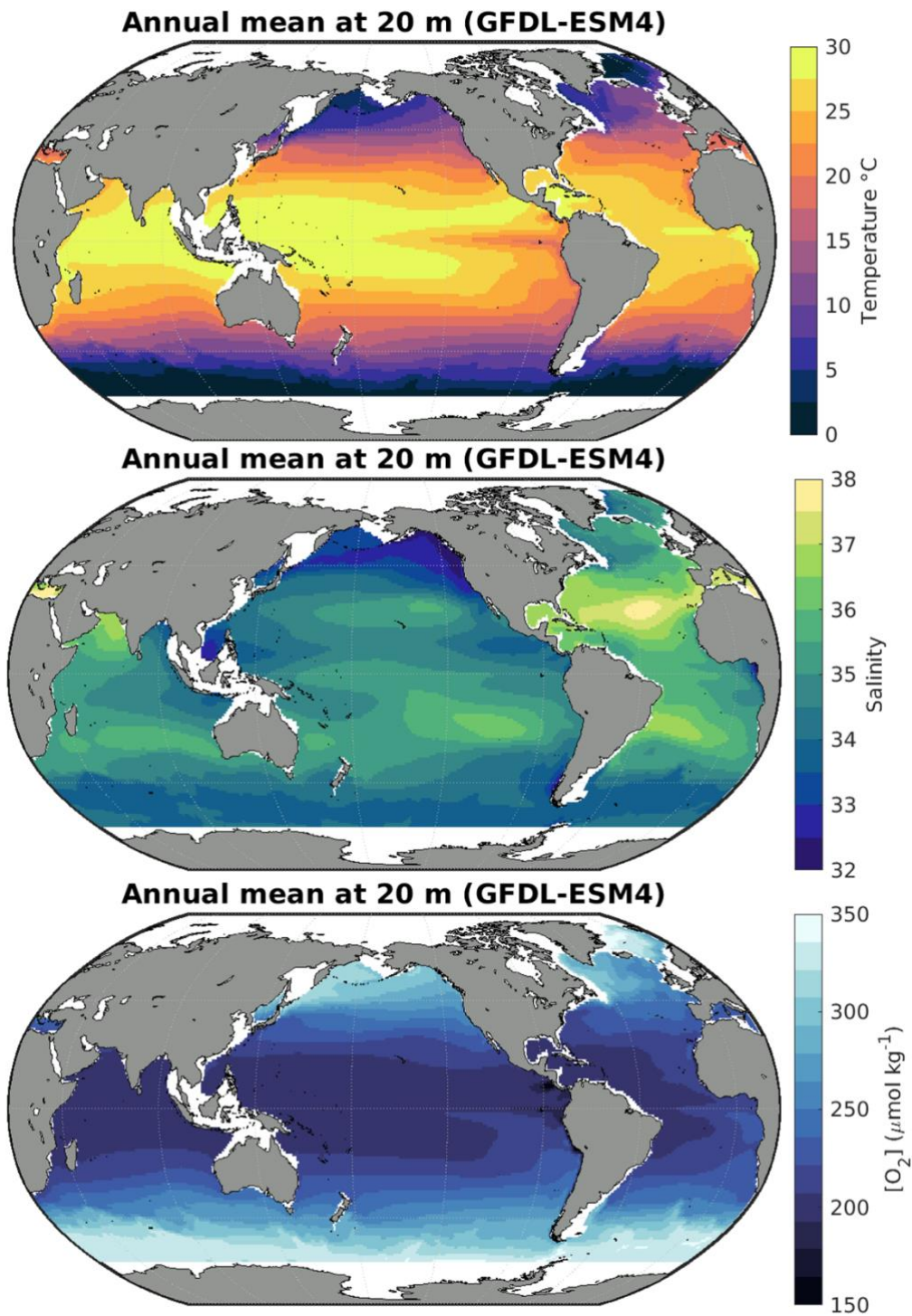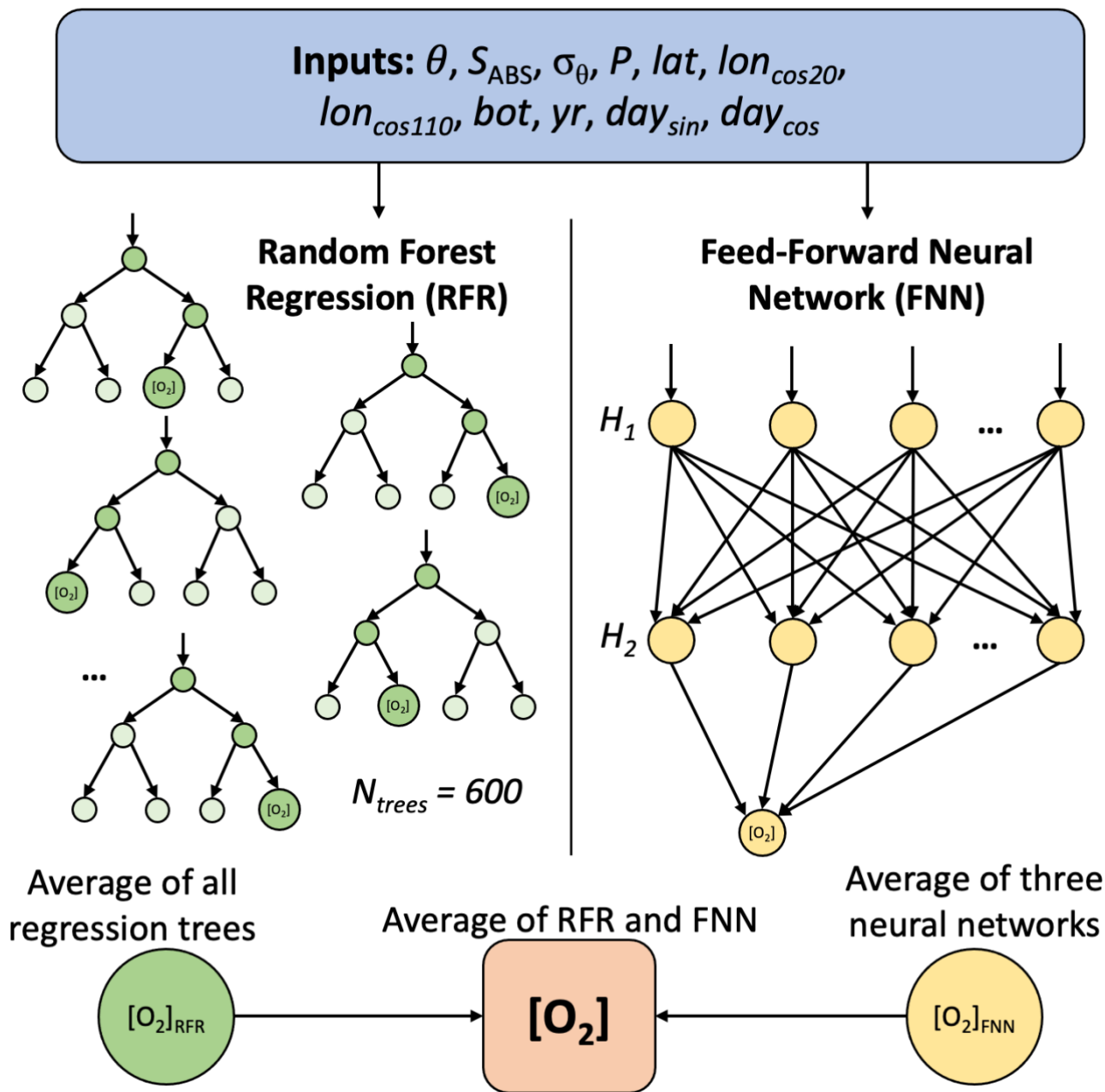
Figure A2. Annual mean in situ temperature (top) and salinity (bottom) from RG09 (2004–2022) at 20 dbars.

Figure A3. Annual mean in situ temperature (top), salinity (middle), and dissolved oxygen concentration (bottom) from GFDL-ESM4 (2004–2021) at 20 meters.

695

30

Inputs: θ, S_{ABS}, σ_θ, P, lat, lon_{cos20}, lon_{cos110}, bot, yr, day_{sin}, day_{cos}

Random Forest Regression (RFR)

Feed-Forward Neural Network (FNN)

H_1

H_2

$[O_2]$

$N_{trees} = 600$

Average of all regression trees

Average of RFR and FNN

Average of three neural networks

$[O_2]_{RFR}$

$[O_2]$

$[O_2]_{FNN}$

Figure A4. A schematic for the random forest regressions (RFRs) and feed-forward neural networks (FNNs). A random subset of the predictors is used for each tree in the RFR, and a randomly chosen predictor is used for each node split. The two hidden layers (H_1 and H_2) in each of the three FNNs have 10 and 20, 15 and 15, and 20 and 10 nodes. Each machine learning algorithm is trained with input data and [O_2] observations, then used to predict [O_2] from new input data.

Training Data

Test Data
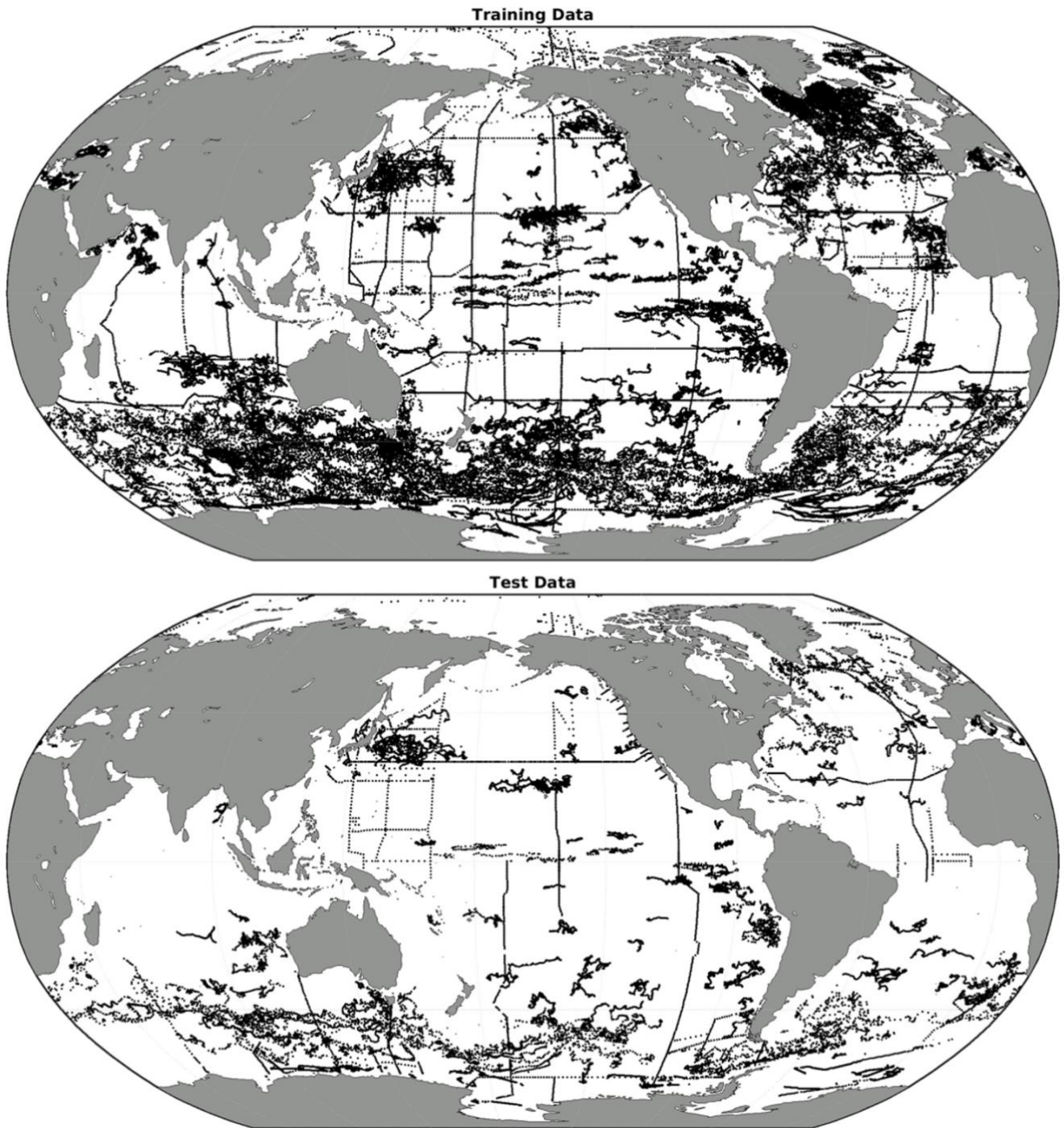
705

Figure A5. The spatial distribution of profile data used to (a) train and (b) test RFR$_{Data-Eval}$ and FNN$_{Data-Eval}$ algorithms.
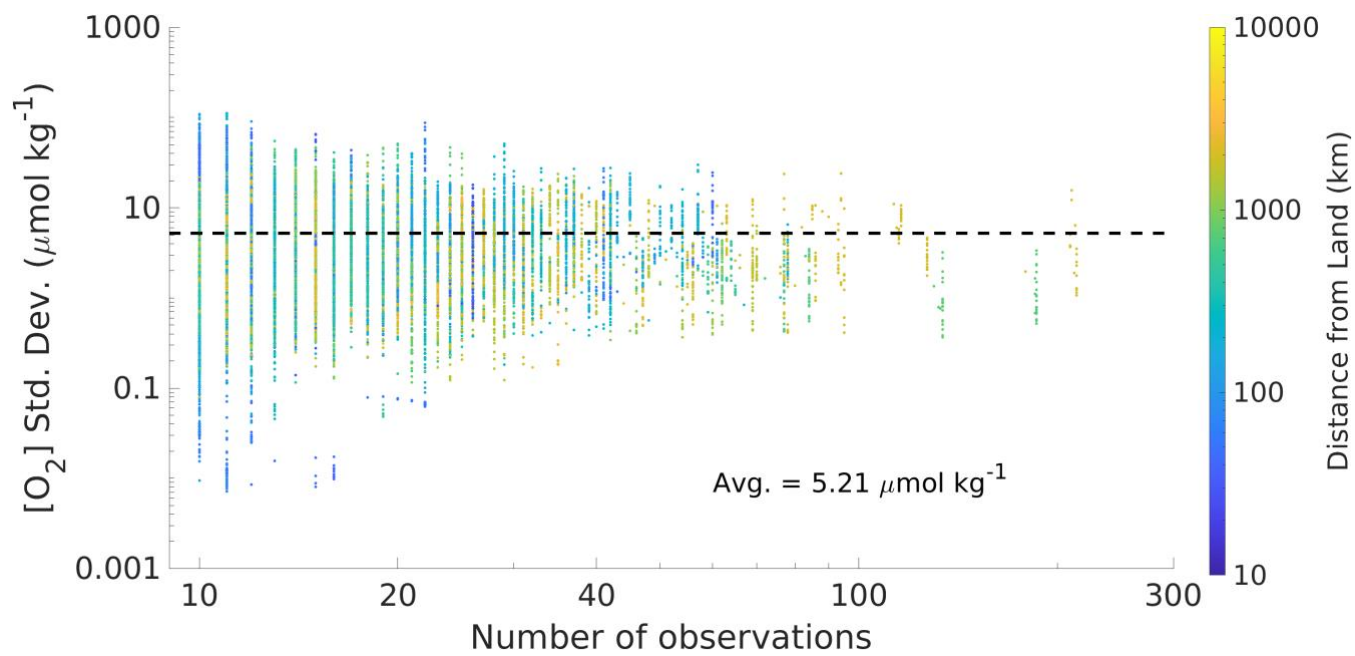
Figure A6. A comparison between the number of observations binned within a four-dimensional grid cell and the standard deviation in [O₂] among those observations. The horizontal black line shows the mean standard deviation (5.21 μmol kg⁻¹).
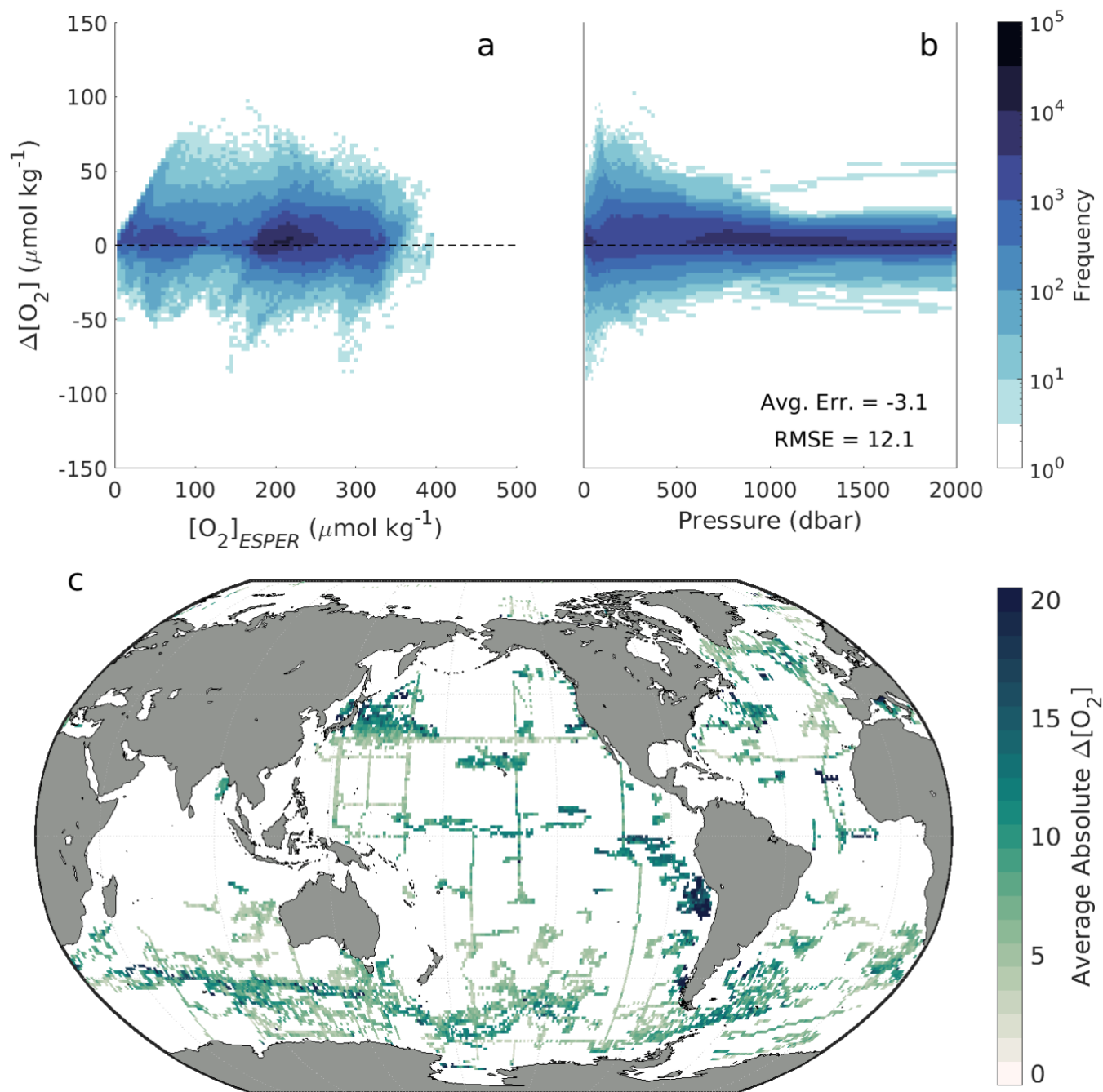
Figure A7. For withheld Argo and GLODAP data, two-dimensional histograms showing offsets between measured and ESPER-Mixed-calculated oxygen ($\Delta[O_2] = [O_2]_{meas} - [O_2]_{ESPER}$) as a function of (a) $[O_2]_{ESPER}$ and (b) pressure in the water column. Offsets are binned into cells that are 2.5 μmol kg^{-1} tall in terms of $\Delta[O_2]$ and 5 μmol kg^{-1} wide in terms of (a) $[O_2]_{ESPER}$ or (b) equivalent in width to the interpolated depth levels of the data. (c) Absolute $\Delta[O_2]$ values averaged over depth and time for 1° latitude by 1° longitude grid cells in the global ocean.
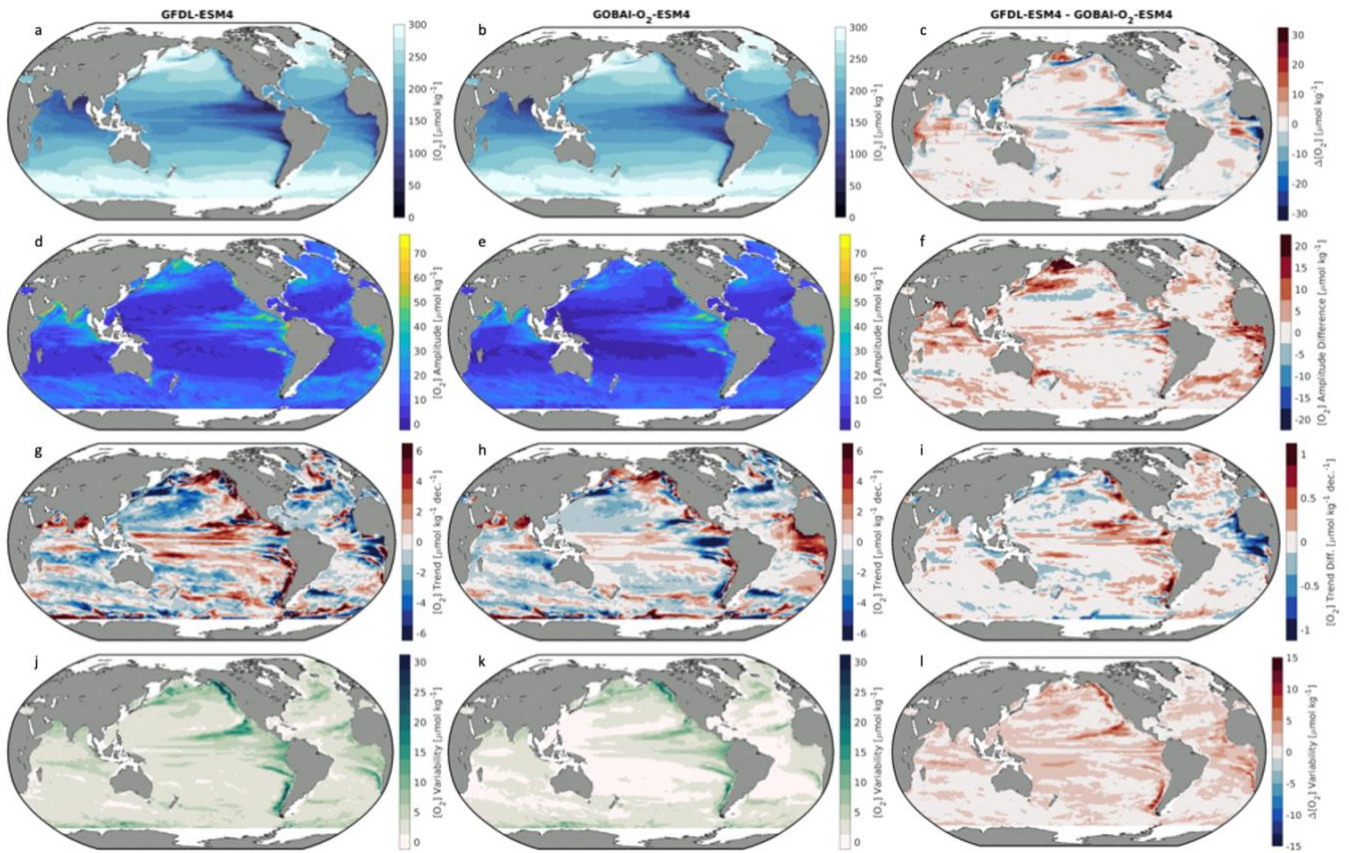
720

Figure A8. Integrated from 0 to 200 dbars: (a,b) long-term mean [O$_2$], (d,e) seasonal [O$_2$] amplitudes, (g,h) trends in [O$_2$], and (j,k) interannual variability in [O$_2$] for (a,d,g,j) GFDL-ESM4 and (b,e,h,k) GOBAI-O$_2$-ESM4, along with (c,f,i,l) the difference between the two.
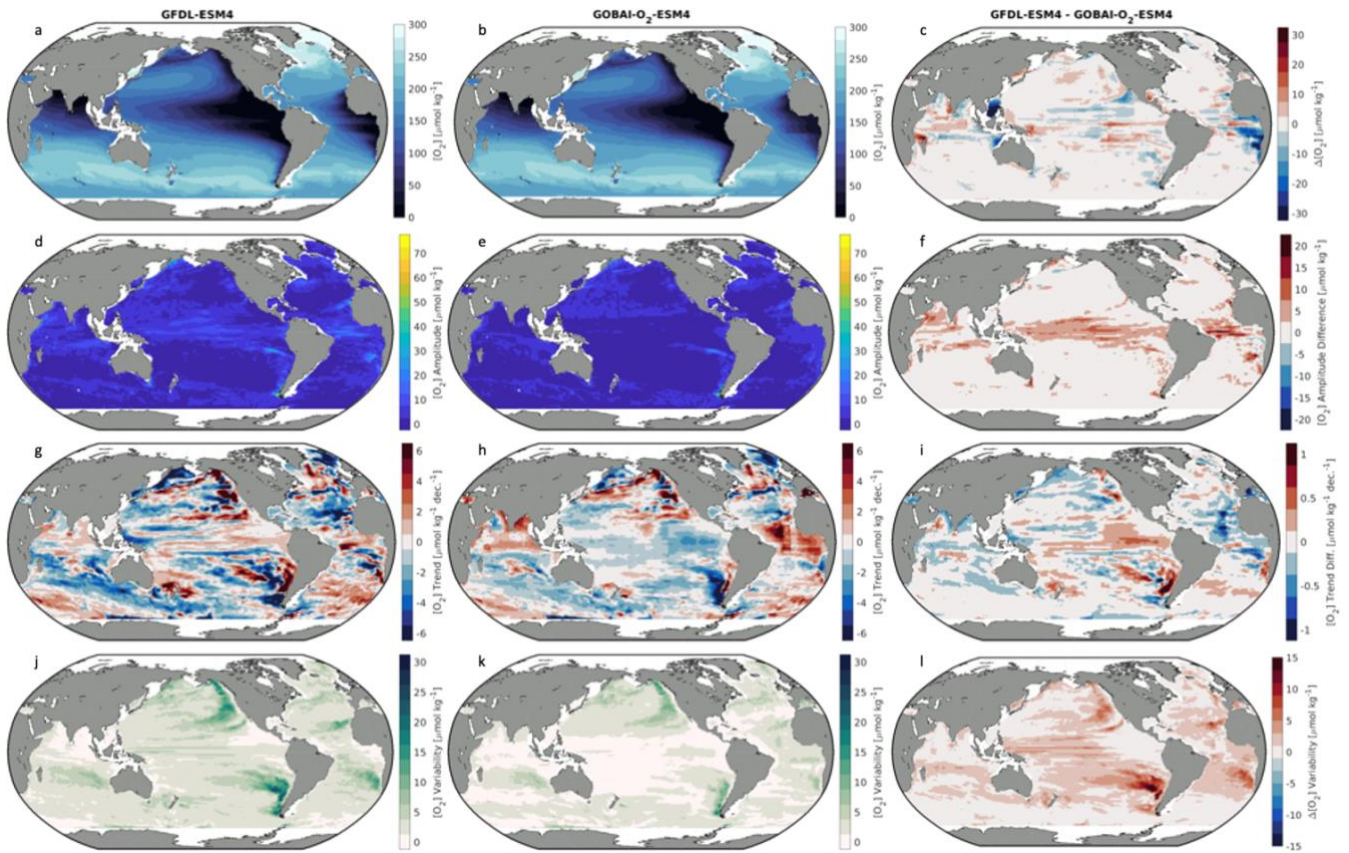
Figure A9. Integrated from 200 to 1000 dbars: (a,b) long-term mean [O_2], (d,e) seasonal [O_2] amplitudes, (g,h) trends in [O_2], and (j,k) interannual variability in [O_2] for (a,d,g,j) GFDL-ESM4 and (b,e,h,k) GOBAI-O_2-ESM4, along with (c,f,i,l) the difference between the two.
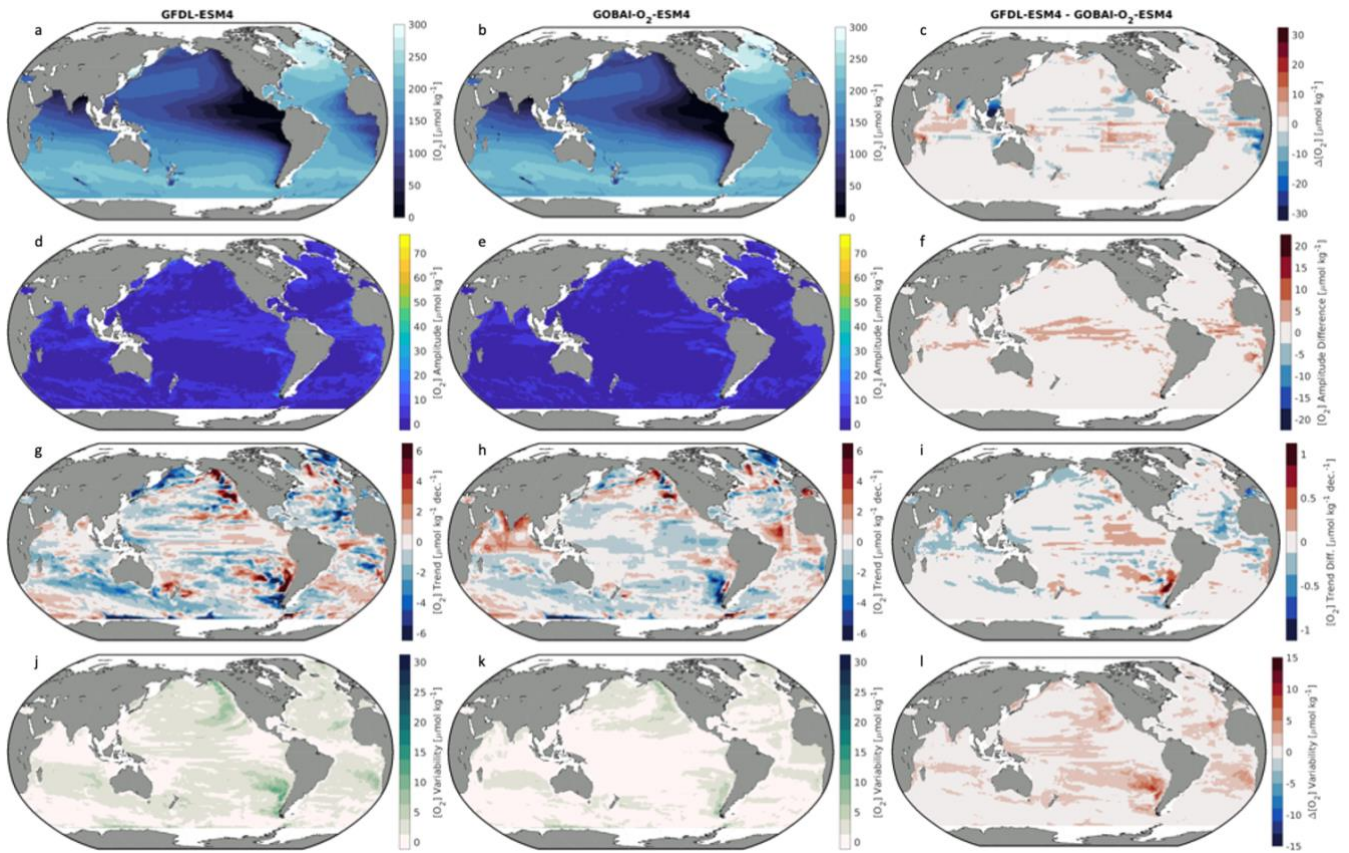
Figure A10. Integrated from 0 to 2000 dbars: (a,b) long-term mean [O$_2$], (d,e) seasonal [O$_2$] amplitudes, (g,h) trends in [O$_2$], and (j,k) interannual variability in [O$_2$] for (a,d,g,j) GFDL-ESM4 and (b,e,h,k) GOBAI-O$_2$-ESM4, along with (c,f,i,l) the difference between the two.
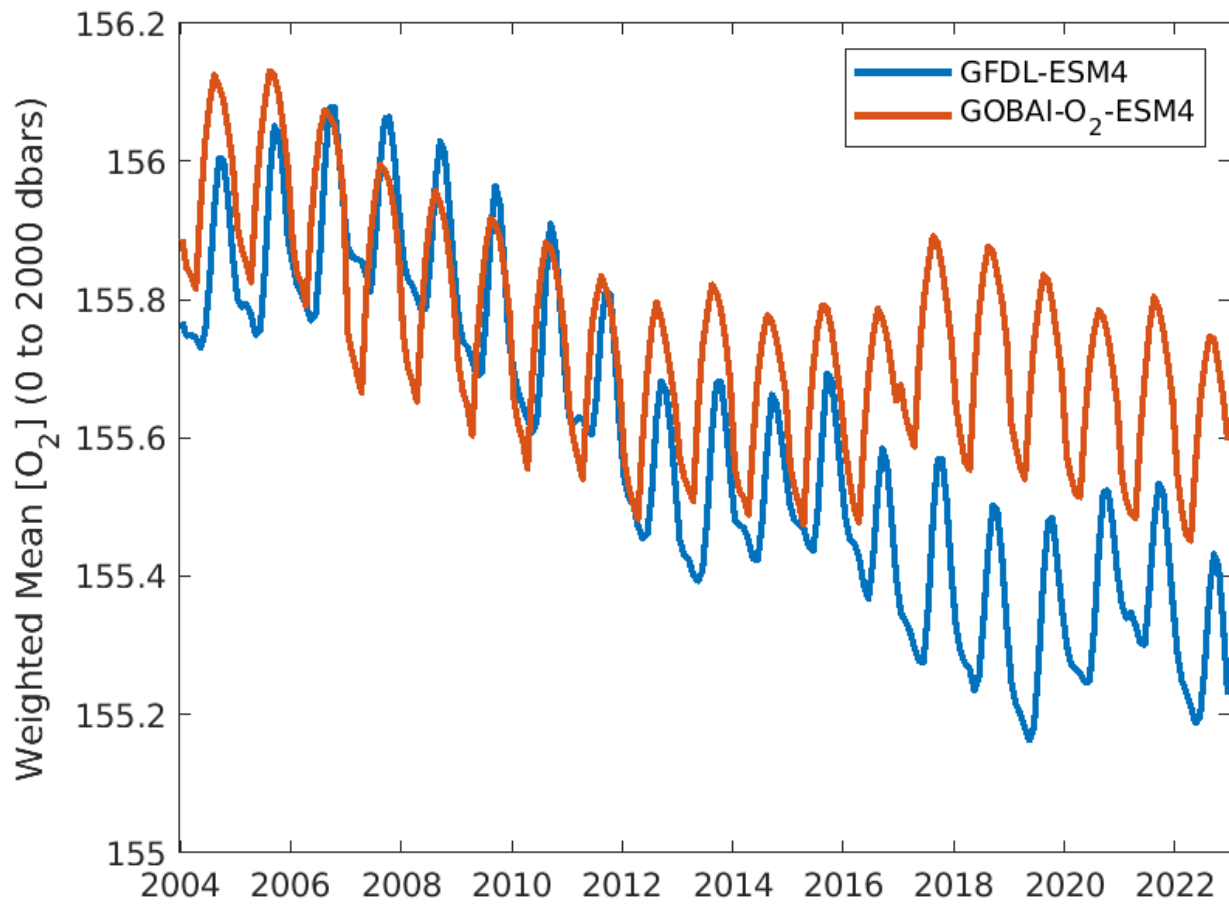
Figure A11. Monthly area-weighted mean [O_2] integrated globally from 0 to 2000 dbars from GFDL-ESM4 (blue) and GOBAI-O_2-ESM4 (orange).

740

Average Surface %O₂ Saturation
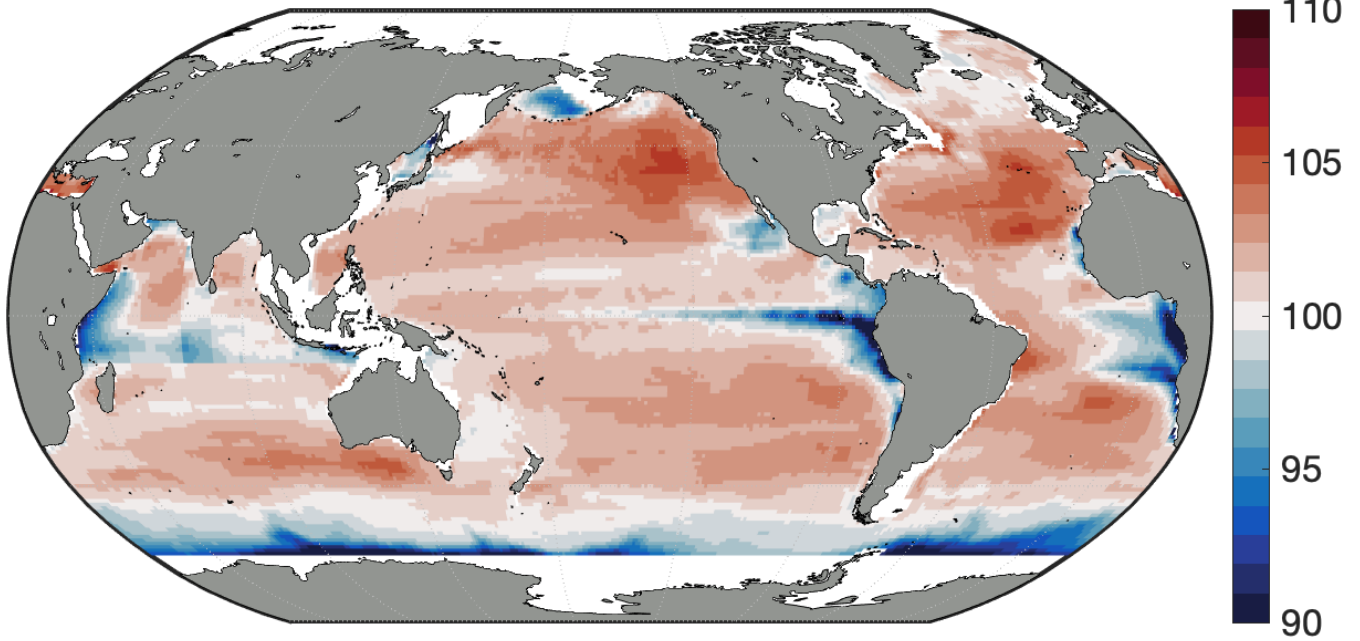
745   **Figure A12.** Long-term mean percent oxygen saturation on the uppermost pressure level in GOBAI-O$_2$.
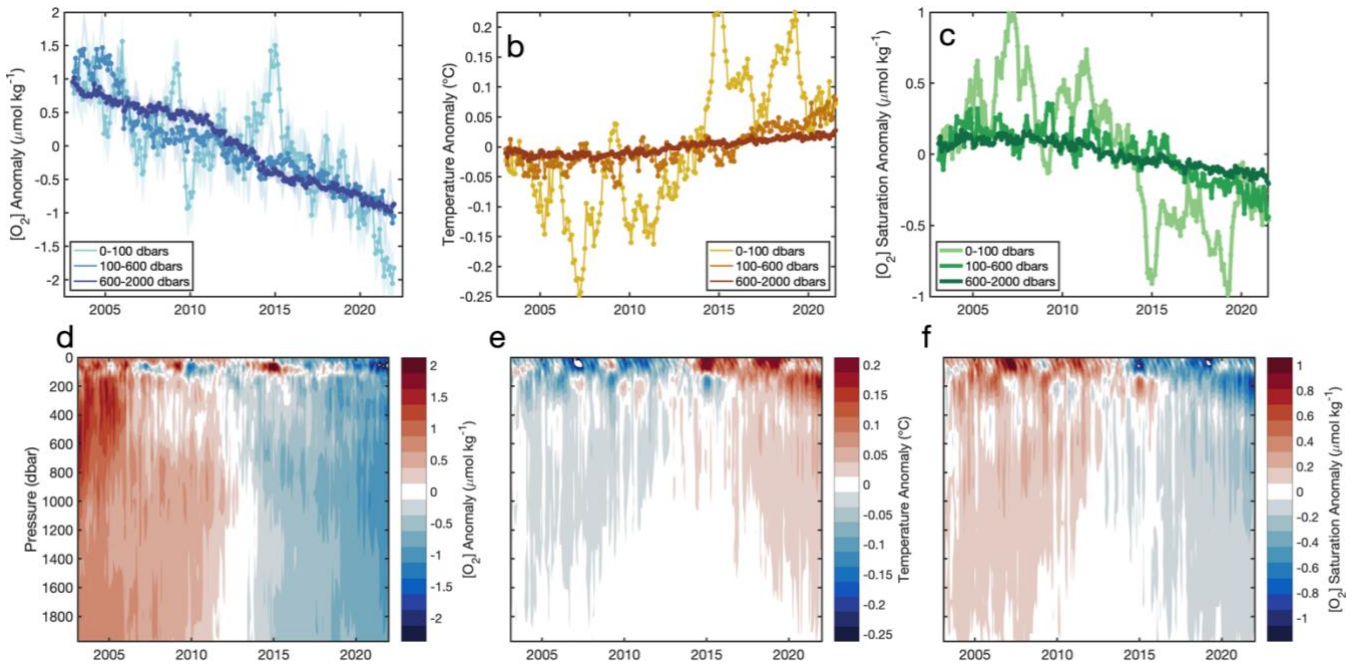
Figure A13. Monthly mean de-seasonalized (a) $[O_2]$ anomalies from GOBAI-O_2, (b) temperature anomalies from RG09, and (c) $[O_2]_{sat.}$ anomalies calculated from RG09 temperature and salinity fields, each integrated globally over three pressure intervals: 0–100, 100–600, and 600–2000 dbars. (a) Shading represents uncertainty determined as the average difference between mean $[O_2]$ from GOBAI-O_2-ESM4 versus GFDL-ESM4 in each interval. Hovmöller diagrams showing monthly mean de-seasonalized (d) $[O_2]$ anomalies from GOBAI-O_2, (e) temperature anomalies from RG09, and (f) $[O_2]_{sat.}$ anomalies calculated from RG09 temperature and salinity fields, each over depth in decibars from 2004 to 2022. Anomalies in each parameter are calculated as monthly mean values with a seasonal cycle removed and minus the long-term mean either (a–c) integrated over a depth interval or (d–f) on a given depth level.
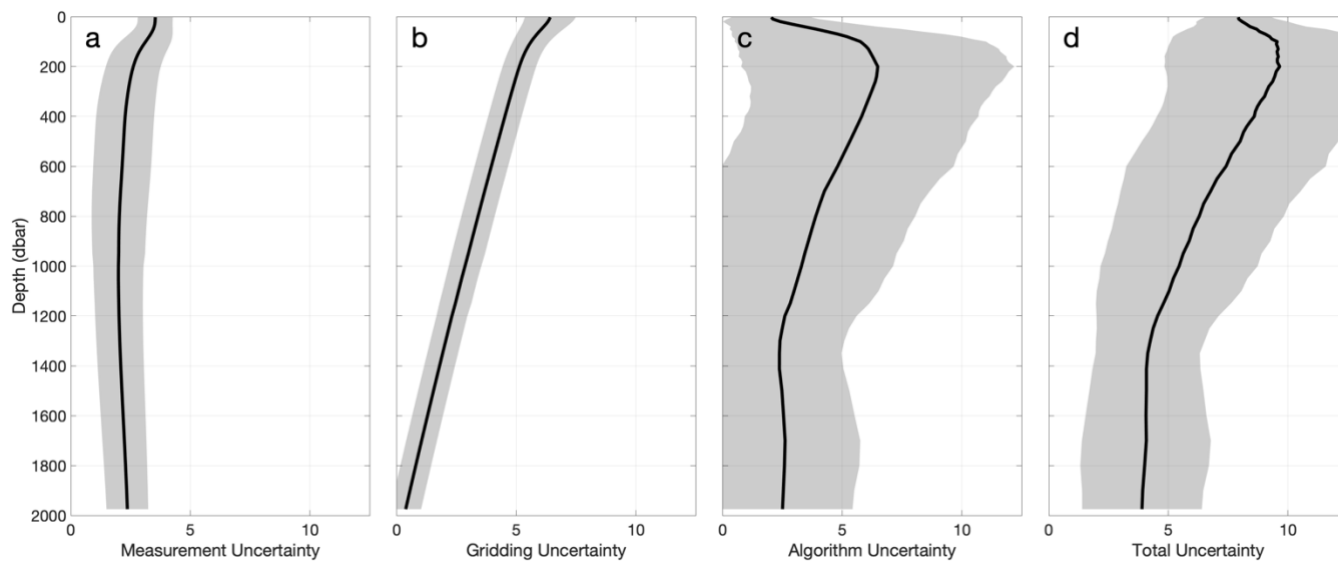
Figure A14. Global mean depth profiles of uncertainty contributors to GOBAI-O$_2$, including (a) measurement uncertainty, (b) gridding uncertainty, (c) algorithm uncertainty, and (d) total uncertainty. The shaded region represents variability in space, and is calculated as the standard deviation on each depth level of the mean uncertainties over time for each grid cell.

760
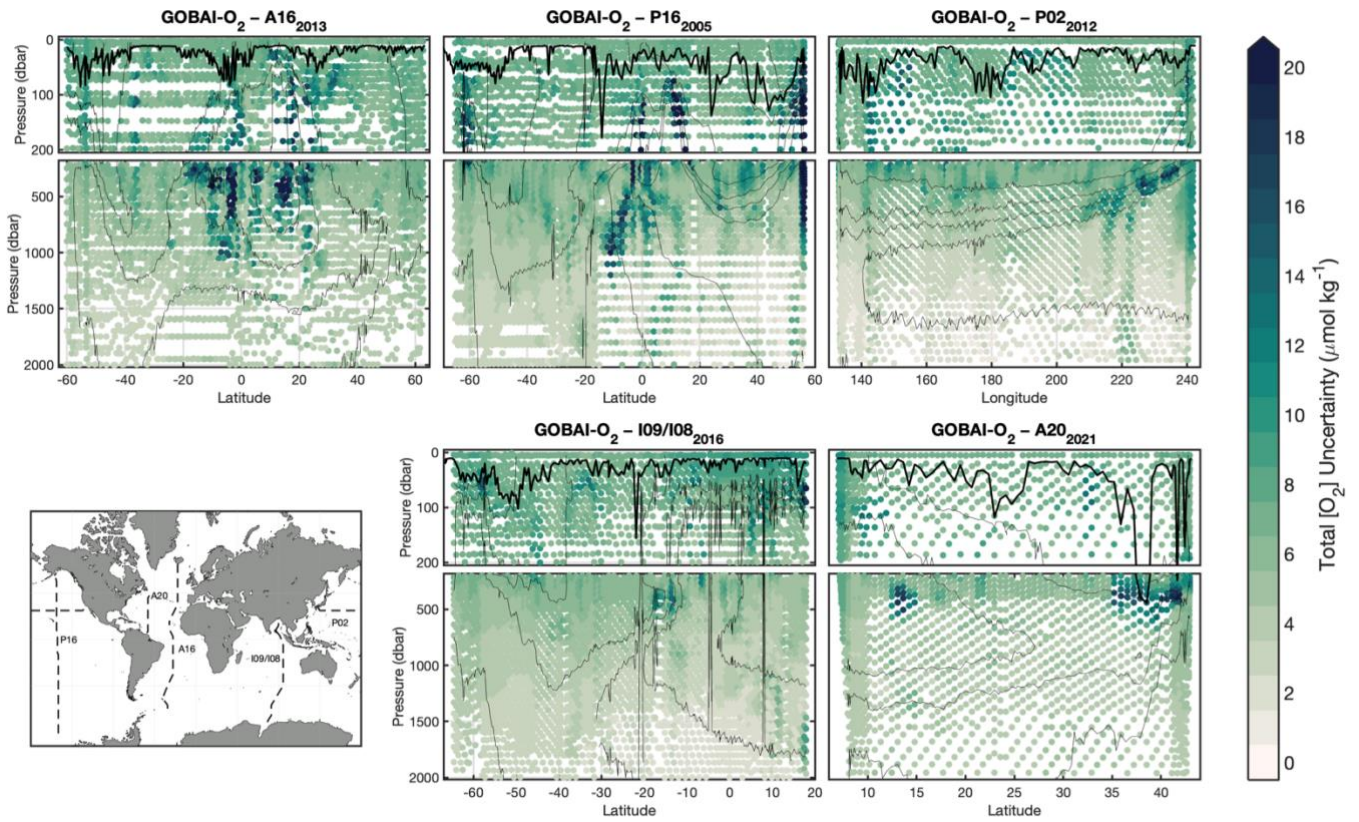
Figure A15. Section plots displaying total uncertainty estimates from GOBAI-O_2 that correspond to discrete measurements of [O_2] from repeat hydrography cruises, to be compared to Δ[O_2] values in Fig. 11.

Appendix B. Supplemental Tables

770 **Table B1.** Boundaries for the seven large ocean regions used to fit machine learning algorithms.

Basin	Polygon Vertices: [Longitude,Latitude; …]
Atl.	[−60,0; −79,9.4; −81,8.4,−100,22;−100,45;−6,45;−6,35;4,15;25,0;22,−35;−68,−35;−60,0]
Pac.*	[104,0;104,70;181,70;181,0;181,−35;145,−35;131,−30;131,0;104,0] [−180,0;−180,70;−150,70;−150,67;−120,67;−100,22; −81,8.4; −79,9.4;−60,0;−68,−35;−180,−35;−180,0]
Ind.	[22,−35;25,10;38,35;104,35;104,0;131,0;131,−30;116,−35;22,−35]
Arc.	[−180,64;−180,90;181,90;181,67;90,67;0,50;0,40;−6,40;−6,35;−90,35;−120,64;−180,64]
Med.	[−6.5,40;0,40;0,45;20,47;38,35;34,30;−5,30;−6.5,40]
N. Sou.	[−180,−60;−180,−25;181,−25;181,−60;−180,−60]
S. Sou.	[−180,−90;−180,−50;181,−50;181,−90;−180,−90]

*Two sets of boundaries are given for the Pacific to accommodate crossing the international date line.

Table B2. Error statistics (mean $\Delta[O_2]$ and RMSD) for tests using RFR and FNN algorithms trained on a subset of Argo and
775 GLODAP data and tested with a separate subset of withheld data. Also shown are error statistics corresponding to the ensemble
average (ENS) of the estimates from both algorithms.

Basin	Training Data Points	Assessment Data Points	RFR$_{\text{Data-Eval}}$		FNN$_{\text{Data-Eval}}$		ENS$_{\text{Data-Eval}}$	
			Mean $\Delta[O_2]$ (μmol kg^{-1})	RMSD (μmol kg^{-1})	Mean $\Delta[O_2]$ (μmol kg^{-1})	RMSD (μmol kg^{-1})	Mean $\Delta[O_2]$ (μmol kg^{-1})	RMSD (μmol kg^{-1})
Atl.	553,272	131,488	−1.2	8.7	−1.2	8.7	−1.2	8.4
Pac.	1,692,647	533,165	−0.2	9.2	−0.1	10.1	−0.1	9.1
Ind.	365,977	50,906	−2.1	8.8	−1.1	7.3	−1.6	7.8
Arc.	919,361	93,191	0.4	8.4	−0.1	9.0	0.2	8.4
Med.	202,690	45,749	−1.8	7.7	−2.2	8.7	−2.0	7.8
N. Sou.	2,125,988	573,925	−0.9	8.8	−1.0	8.3	−0.9	8.3
S. Sou.	1,399,346	374,952	−0.3	7.4	−0.3	7.6	−0.3	7.3
All	7,259,281	1,803,376	−0.7	8.8	−0.6	9.0	−0.6	8.6

The header above "Evaluation Exercise with Observational Data" spans the data columns.

Table B3. Error statistics (mean Δ[O₂] and RMSD) for tests using RFR and FNN algorithms trained on a subset of output from GFDL-ESM4 (corresponding to locations of available Argo and GLODAP data) and tested using a separate subset of withheld output from GDFL-ESM4. Also shown are error statistics corresponding to the ensemble average (ENS) of the estimates from both algorithms.

Basin	Training Data Points	Assessment Data Points	RFR$_{\text{ESM4-Eval}}$		FNN$_{\text{ESM4-Eval}}$		ENS$_{\text{ESM4-Eval}}$	
			Mean Δ[O₂] (μmol kg^{-1})	RMSD (μmol kg^{-1})	Mean Δ[O₂] (μmol kg^{-1})	RMSD (μmol kg^{-1})	Mean Δ[O₂] (μmol kg^{-1})	RMSD (μmol kg^{-1})
Atl.	179,322	28,235,064	−1.9	12.1	0.4	9.5	−0.7	9.0
Pac.	522,834	69,369,456	0.2	7.4	−0.4	8.9	−0.1	7.5
Ind.	85,748	20,736,144	0.7	8.7	−0.2	7.4	0.3	6.9
Arc.	281,684	11,547,744	0.1	4.2	−0.3	4.8	−0.1	4.2
Med.	32,110	1,096,680	0.8	4.8	1.3	7.5	1.0	5.5
N. Sou.	752,856	67,626,624	0.0	4.3	−0.1	4.9	−0.1	4.3
S. Sou.	515,502	31,412,472	0.1	3.3	−0.1	3.6	0.0	3.3
All	2,370,056	230,024,184	−0.1	7.5	−0.1	7.5	−0.1	6.6

Table B4. Error statistics (mean Δ[O₂] and RMSD) for tests using RFR and FNN algorithms trained on a subset of Argo and GLODAP data and tested with all available GLODAP data. Also shown are error statistics corresponding to the ensemble average (ENS) of the estimates from both algorithms and corresponding to the ESPER-Mixed model (Carter et al., 2021).

Basin	Training Data Points	Assessment Data Points	RFR$_{\text{Data-Eval}}$		FNN$_{\text{Data-Eval}}$		ENS$_{\text{Data-Eval}}$		ESPER-Mixed	
			Mean Δ[O₂] (μmol kg^{-1})	RMSD (μmol kg^{-1})	Mean Δ[O₂] (μmol kg^{-1})	RMSD (μmol kg^{-1})	Mean Δ[O₂] (μmol kg^{-1})	RMSD (μmol kg^{-1})	Mean Δ[O₂] (μmol kg^{-1})	RMSD (μmol kg^{-1})
Atl.	553,272	180,374	0.4	4.9	0.6	8.9	0.5	6.4	0.1	11.3
Pac.	1,692,647	495,035	0.7	6.3	1.2	9.5	1.0	7.3	−0.3	11.0
Ind.	365,977	42,460	0.5	3.9	1.0	7.2	0.7	5.2	−1.3	9.2
Arc.	919,361	227,905	0.1	4.4	0.2	8.6	0.2	6.0	1.2	11.0
Med.	202,690	60	−2.0	5.3	2.4	8.5	0.2	5.8	−5.5	7.7
N. Sou.	2,125,988	174,368	0.3	5.4	0.4	7.5	0.4	6.1	−0.7	8.4
S. Sou.	1,399,346	141,065	−0.1	5.1	−0.5	8.0	−0.3	6.1	−0.3	9.5
All	7,259,281	1,261,267	0.4	5.6	0.7	8.9	0.6	6.8	0.0	10.7

Table B5. Estimated decadal trends and uncertainties in [O₂] (μmol kg⁻¹ dec.⁻¹) and oxygen inventory (% dec.⁻¹) in different depth intervals of GOBAI-O₂. Uncertainties are determined according to the procedure in Appendix E, both using the autocorrelation of residuals to the linear least squares model (Autocov.) and by incorporating estimated uncertainty in global mean GOBAI-O₂ fields (u(ESM4)). The value used to represent uncertainty on each trend (larger value) is in bold.

Depth Interval	[O₂] Trend (μmol kg⁻¹ dec.⁻¹)	Trend Uncertainty (μmol kg⁻¹ dec.⁻¹)		O₂ Inventory Trend (% dec.⁻¹)	Trend Uncertainty (% dec.⁻¹)	
		Autocov.	u(ESM4)		Autocov.	u(ESM4)
0 – 100 dbar	−1.00	**0.51**	0.42	−0.45	**0.23**	0.19
100 – 600 dbar	−1.09	**0.34**	0.33	−0.68	**0.21**	0.21
600 – 2000 dbar	−1.06	0.23	**0.36**	−0.75	0.16	**0.26**
0 – 1000 dbar	−1.12	0.15	**0.21**	−0.72	0.09	**0.13**
0 – 2000 dbar	−1.06	0.08	**0.20**	−0.71	0.06	**0.13**

795

Table B6. Summary error statistics between direct observations from repeat hydrography cruises and GOBAI-O₂ and WOA18.

Cruise	GOBAI-O₂		WOA18	
	Mean Δ[O₂]	RMSD	Mean Δ[O₂]	RMSD
A16 (2013)	−0.3	9.3	0.2	12.0
P16 (2005)	0.1	14.7	0.2	14.5
P02 (2012)	−1.0	9.8	−0.4	12.9
I08/I09 (2016)	−2.3	10.9	−1.1	13.0
A20 (2021)	−7.3	22.9	−2.2	21.4

Appendix C. Supplemental Datasets

1. The original and vertically interpolated observational datasets from the BGC Argo and GLODAP databases that are used to develop GOBAI-O$_2$ can be found at https://doi.org/10.5281/zenodo.7747237 (Sharp, 2023a).

2. The algorithms trained on vertically interpolated observational data that were applied to predictor variables to produce GOBAI-O$_2$ can be found at https://doi.org/10.5281/zenodo.7747308 (Sharp, 2023b).

Appendix D. Float Data Adjustments

805   A negative median bias (-1.25 μmol kg^{-1}) in float [O_2] measurements compared to co-located ship [O_2] measurements (below 300 dbars only to avoid the impact of high frequency variability near the surface) was adjusted by fitting the differences (Δ[O_2]) to a linear least squares model as a function of float [O_2], and adding that [O_2]-dependent adjustment back on to the float [O_2] measurements. The Δ[O_2] values as a function of float [O_2] before (a) and after (b) this adjustment are shown in the Figure D1. This resulted in a reduced median Δ[O_2] of 0.34 μmol kg^{-1}.

810
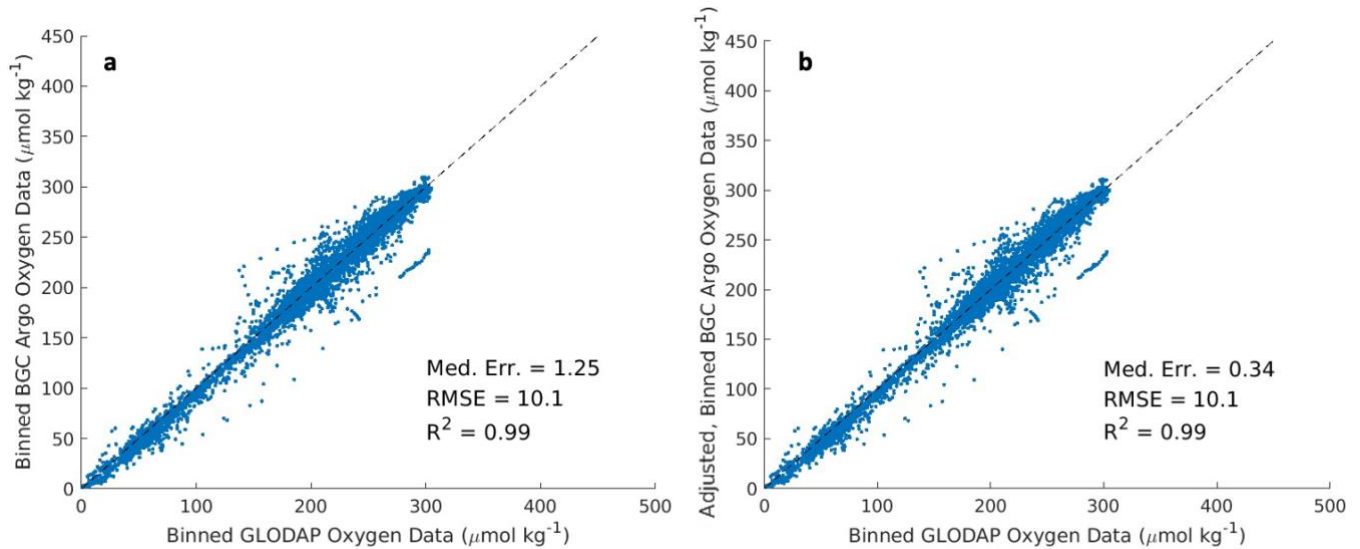
Figure D1. Unadjusted (a) and adjusted (b) matchups between BGC Argo [O_2] measurements (y-axis) versus GLODAP [O_2]
815   measurements (x-axis). The adjustment procedure doesn't mitigate the scatter between the matchups, but does reduce the median error.

Appendix E. Determination of Trends

Trends and associated uncertainties in GOBAI-O_2 were determined via the following procedure:

1. Spatially weighted monthly mean [O_2] values for the entire GOBAI-O_2 domain or within specified depth intervals were calculated from gridded [O_2], using relative grid cell volumes as weights.

2. A linear least squares model with a trend, intercept, and annual (12-month) and semi-annual (6-month) periods was fit to monthly mean [O_2] values. The monthly trend from the least squares model was multiplied by 120 to obtain a **decadal trend of weighted mean [O_2]**.

3. Uncertainty on the decadal trends were assessed in two different ways, and the largest of the two uncertainty estimates taken for each analyzed depth interval, indicating that either (a) uncertainty in the linear least squares model or (b) uncertainty in the GOBAI-O_2 fields was driving uncertainty in the trend. The two methods were as follows:

    a. Using the autocovariance of residuals from the linear least squares model:

        i. The standard error on the trend was calculated from the covariance matrix of the linear least squares model.

        ii. The autocovariance of the residuals from the least squares model was examined to compute the e-folding timescale, and the effective degrees of freedom were obtained by dividing the number of monthly mean [O_2] values by the e-folding timescale.

        iii. The standard error on the trend was scaled by the effective degrees of freedom, multiplied by 2 to obtain a 90% confidence interval, and multiplied by 120 to obtain an **uncertainty on the decadal trend of weighted mean [O_2]**.

    b. By incorporating estimated uncertainty in global mean GOBAI-O_2 fields:

        i. Uncertainties in monthly mean [O_2] values were determined as standard deviations of monthly differences between GOBAI-O_2-ESM4 and GFDL-ESM4 (section 3.1.2).

        ii. These uncertainties were used to compute a weight matrix for the linear least squares fit.

        iii. The standard error on the trend was scaled by the effective degrees of freedom, multiplied by 2 to obtain a 90% confidence interval, and multiplied by 120 to obtain an **uncertainty on the decadal trend of weighted mean [O_2]**.

4. The process was repeated for oxygen inventories for the entire GOBAI-O_2 domain or within each specified depth interval; inventories were determined from gridded [O_2], volumes of each grid cell, and densities of each grid cell.

48

6 Data availability

GOBAI-O$_2$ is available as a NetCDF file at https://doi.org/10.25921/z72m-yz67 (Sharp et al., 2023; last access: 19 Mar. 2023). GLODAPv2 is updated annually and is available at www.glodap.info. GFDL-ESM4 model output can be accessed via the World Climate Research Programme database (https://esgf-node.llnl.gov/projects/cmip6/). Data from the 2018 World Ocean Atlas can be accessed through NOAA NCEI (https://www.ncei.noaa.gov/products/world-ocean-atlas). The OneArgo-Mat toolbox used to download Argo float data is available at https://doi.org/10.5281/zenodo.6588041; the toolbox acquires data from two global data assembly centers: Coriolis (ftp://ftp.ifremer.fr/ifremer/argo) and US-GODAE (ftp://usgodae.org/pub/outgoing/argo). The Roemmich and Gilson (2009) Argo-based temperature and salinity product is available at https://sio-argo.ucsd.edu/RG_Climatology.html.

7 Author contributions

JDS, AJF, BRC, and GCJ conceptualized and planned the project. JDS produced the data product, conducted all analysis, created the data visualizations, and wrote the original draft of the manuscript. JDS, AJF, BRC, GCJ, JPD, and CS reviewed and edited the manuscript.

8 Competing interests

The authors declare no competing interests.

9 Acknowledgements

10 References

Alkire, M. B., D'Asaro, E., Lee, C., Perry, M. J., Gray, A., Cetinić, I., Briggs, N., Rehm, E., Kallin, E., Kaiser, J., González-Posada, A. Estimates of net community production and export using high-resolution, Lagrangian measurements of O_2, NO_3^-, and POC through the evolution of a spring diatom bloom in the North Atlantic. Deep Sea Res. I 64, 157–174, https://doi.org/10.1016/j.dsr.2012.01.012, 2012.

Arteaga, L. A., Pahlow, M., Bushinsky, S. M., Sarmiento, J. L. Nutrient controls on export production in the Southern Ocean. Glob. Biogeochem. Cycl. 33, 942–956, https://doi.org/10.1029/2019GB006236, 2019.

Berman-Frank, I., Chen, Y. B., Gao, Y., Fennel, K., Follows, M. J., Milligan, A. J., Falkowski, P. G. Feedbacks between the nitrogen, carbon and oxygen cycles. In *Nitrogen in the Marine Environment*. Elsevier Inc., 1539–1563, 10.1016/B978-0-12-372522-6.00035-3, 2008.

Bindoff, N. L., Cheung, W.W.L., Kairo, J.G. et al. Changing ocean, marine ecosystems, and dependent communities. In *IPCC Special Report on the Ocean and Cryosphere in a Changing Climate*, ed. H.-O. Pörtner, C.D. Roberts, V. Masson-Delmotte, P. Zhai, E. Tignor, E. Poloczanska, K. Mintenbeck, A. Alegria, et al., 447–588, https://doi.org/10.1017/9781009157964, 2019.

Bittig, H. C., Fiedler, B., Scholz, R., Krahmann, G., Körtzinger, A. Time response of oxygen optodes on profiling platforms and its dependence on flow speed and temperature. Limnol. Oceanogr.: Methods, 12, 617–636, https://doi.org/10.4319/lom.2014.12.617, 2014.

Bittig, H. C., Körtzinger, A. Tackling oxygen optode drift: Near-surface and in-air oxygen optode measurements on a float provide an accurate in situ reference. J. Atmos. Oce. Technol., 32, 1536-1543, https://doi.org/10.1175/JTECH-D-14-00162.1, 2015.

Bittig, H. C., Körtzinger, A. Technical note: Update on response times, in-air measurements, and in situ drift for oxygen optodes on profiling platforms. Ocean Science 13, 1–11, https://doi.org/10.5194/os-13-1-2017, 2017.

Bittig, H. C., Körtzinger, A., Neill, C., van Ooijen, E., Plant, J. N., Hahn, J., Johnson, K. S., Yang, B., Emerson, S. R. Oxygen optode sensors: Principle, characterization, calibration, and application in the ocean. Front. Mar. Sci. 4, 429, https://doi.org/10.3389/fmars.2017.00429, 2018a.

Bittig, H. C., Steinhoff, T., Claustre, H., Fiedler, B., Williams, N. L., Sauzède, R., Körtzinger, A., Gattuso, J. P. An alternative to static climatologies: Robust estimation of open ocean CO_2 variables and nutrient concentrations from T, S, and O_2 data using Bayesian neural networks. Front. Mar. Sci. 5, 328, https://doi.org/10.3389/fmars.2018.00328, 2018b.

Bittig, H., Wong, A., Plant, J. BGC-Argo synthetic profile file processing and format on Coriolis GDAC. Ifremer, Plouzane, France, https://doi.org/10.13155/55637, 2022.

Bopp, L., Resplandy, L., Orr, J. C., Doney, S. C., Dunne, J. P., Gehlen, M., Halloran, P., Heinze, C., Ilyina, T., Séférian, R., Tjiputra, J., Vichi, M. Multiple stressors of ocean ecosystems in the 21st century: Projections with CMIP5 models. Biogeosciences 10, 6225–6245, https://doi.org/10.5194/bg-10-6225-2013, 2013.

Boyer, T. P., Baranova, O. K., Coleman, C., Garcia, H. E., Grodsky, A., Locarnini, R. A., Mishonov, A. V., Paver, C. R., Reagan, J. R., Seidov, D., Smolyar, I. V., Weathers, K., Zweng, M. M. World Ocean Database 2018. A.V. Mishonov, Technical Ed., NOAA Atlas NESDIS 87, 2018.

Breiman, L. Random forests, Mach. Learn., 45, 5–32, https://doi.org/10.1023/A:1010933404324, 2001.

Breitburg, D., Levin, L. A., Oschlies, A., Grégoire, M., Chavez, F. P., Conley, D. J., ... Zhang, J. Declining oxygen in the global ocean and coastal waters. Science, 359, 10.1126/science.aam7240, 2018.

Bushinsky, S. M., Emerson, S. Marine biological production from in situ oxygen measurements on a profiling float in the subarctic Pacific Ocean. Glob. Biogeochem. Cycl. 29, 2050–2060, https://doi.org/10.1002/2015GB005251, 2015.

Bushinsky, S. M., Emerson, S. R., Riser, S. C., Swift, D. D. Accurate oxygen measurements on modified Argo floats using in situ air calibrations. Limnol. Oceanogr.: Methods 14, 491–505, https://doi.org/10.1002/lom3.10107, 2016.

Bushinsky, S. M., Gray, A. R., Johnson, K. S., Sarmiento, J. L. Oxygen in the Southern Ocean from Argo floats: Determination of processes driving air-sea fluxes. JGR: Oceans, 122, 8661–8682, https://doi.org/10.1002/2017JC012923, 2017.

Bushinsky, S. M., Emerson, S. R. Biological and physical controls on the oxygen cycle in the Kuroshio Extension from an array of profiling floats. Deep Sea Res. I, 141, 51–70, https://doi.org/10.1016/j.dsr.2018.09.005, 2018.

Carpenter, J. H. The Chesapeake Bay Institute technique for the Winkler dissolved oxygen method. Limnol. Oceanogr. 10, 141–143, https://doi.org/10.4319/lo.1965.10.1.0141, 1965.

Carter, B. R., Bittig, H. C., Fassbender, A. J., Sharp, J. D., Takeshita, Y., Xu, Y. Y., Álvarez, M., Wanninkhof, R., Feely, R. A., Barbero, L. New and updated global empirical seawater property estimation routines. Limnol. Oceanogr.: Methods 19, 785–809, https://doi.org/10.1002/lom3.10461, 2021.

Chierici, M., Fransson, A., Turner, D. R., Pakhomov, E. A., Froneman, P. W. Variability in pH, fCO2, oxygen and flux of CO2 in the surface water along a transect in the Atlantic sector of the Southern Ocean. Deep Sea Res. II 51, 2773–2787, https://doi.org/10.1016/j.dsr2.2001.03.002, 2004.

Claustre, H., Johnson, K. S., Takeshita, Y. Observing the global ocean with biogeochemical-Argo. Annual Rev. Mar. Sci., 12, 23–48, 10.1146/annurev-marine-010419-010956, 2020.

D'Asaro, E. A., McNeil, C. Calibration and stability of oxygen sensors on autonomous floats. J. of Atmos. Oce. Technol. 30, 1896–1906, https://doi.org/10.1175/JTECH-D-12-00222.1, 2013.

Demuth, H., Beale, M., Hagan, M.: Neural Network Toolbox 6 User's Guide, The MathWorks, Inc., 3 Apple Hill Drive, Natick, MA, 2008.

Djeutchouang, L. M., Chang, N., Gregor, L., Vichi, M., Monteiro, P. M. S. The sensitivity of pCO2 reconstructions to sampling scales across a Southern Ocean sub-domain: a semi-idealized ocean sampling simulation approach. Biogeosciences 19, 4171–4195, https://doi.org/10.5194/bg-19-4171-2022, 2022.

Drucker, R., Riser, S. C. In situ phase-domain calibration of oxygen Optodes on profiling floats. Methods in Oceanography 17, 296–318. https://doi.org/10.1016/j.mio.2016.09.007, 2016.

Dunne, J. P., Horowitz, L. W. , Adcroft, A. J., Ginoux, P. , Held, I. M., John, J. G., Krasting, J. P., Malyshev, S., Naik, V., Paulot, F., Shevliakova, E., Stock, C. A., Zadeh, N., Balaji, V., Blanton, C., Dunne, K. A., Dupuis, C., Durachta, J., Dussin, R., Gauthier, P. P. G., Griffies, S. M., Guo, H., Hallberg, R. W., Harrison, M., He, J., Hurlin, W., McHugh, C., Menzel, R., Milly, P. C. D., Nikonov, S., Paynter, D. J., Ploshay, J., Radhakrishnan, A., Rand, K., Reichl, B. G., Robinson, T., Schwarzkopf, D. M., Sentman, L. A., Underwood, S., Vahlenkamp, H., Winton, M., Wittenberg, A. T., Wyman, B., Zeng,

Y., Zhao, M. The GFDL Earth System Model version 4.1 (GFDL-ESM4.1): Model description and simulation characteristics. J. Adv. Model. Earth Syst. 12, e2019MS002015, https://doi.org/10.1029/2019MS002015, 2020.

975   Estapa M. L., Feen M. L., Breves E. Direct observations of biological carbon export from profiling floats in the subtropical North Atlantic. Glob. Biogeochem. Cycles 33, 282–300, https://doi.org/10.1029/2018GB006098, 2019.

Fay, A. R., McKinley, G. A. Global open-ocean biomes: mean and temporal variability. Earth Syst. Sci. Data 6, 273–284, https://doi.org/10.5194/essd-6-273-2014, 2014.

980   Fiedler, B., Fietzek, P., Vieira, N., Silva, P., Bittig, H. C., Körtzinger, A. In Situ CO_2 and O_2 Measurements on a Profiling Float. J. Atmos. Ocean. Tech. 30, 112–126, https://doi.org/10.1175/JTECH-D-12-00043.1, 2013.

Frenzel, H., Sharp, J. D., Fassbender, A. J., Buzby, N. OneArgo-Mat: A MATLAB toolbox for accessing and visualizing Argo data (v1.0.2), Zenodo, https://doi.org/10.5281/zenodo.6588041, 2022.

985

Frölicher, T. L., Joos, F., Plattner, G. K., Steinacher, M., Doney, S. C. Natural variability and anthropogenic trends in oceanic oxygen in a coupled carbon cycle–climate model ensemble. Global Biogeochemical Cycles 23, https://doi.org/10.1029/2008GB003316, 2009.

990   Garcia, H. E., Gordon, L. I. Oxygen solubility in seawater: Better fitting equations. Limnol. Oceanogr., 37, 1307–1312, https://doi.org/10.4319/lo.1992.37.6.1307, 1992.

Garcia, H. E., Weathers, K. W., Paver, C. R., Smolyar, I., Boyer, T. P., Locarnini, M. M., ... Seidov, D. World Ocean Atlas 2018, Volume 3: Dissolved Oxygen, Apparent Oxygen Utilization, and Dissolved Oxygen Saturation, NOAA Atlas NESDIS 995   83, https://archimer.ifremer.fr/doc/00651/76337, 2019.

Garcia-Soto, C., Cheng, L., Caesar, L., Schmidtko, S., Jewett, E. B., Cheripka, A., Rigor, I., Caballero, A., Chiba, S., Báez, J. C., Zielinski, T., Abraham, J. P. An Overview of Ocean Climate Change Indicators: Sea Surface Temperature, Ocean Heat Content, Ocean pH, Dissolved Oxygen Concentration, Arctic Sea Ice Extent, Thickness and Volume, Sea Level and Strength 1000   of the AMOC (Atlantic Meridional Overturning Circulation). Front. Mar. Sci. 8, 642372, https://doi.org/10.3389/fmars.2021.642372, 2021.

Giglio, D., Lyubchich, V., Mazloff, M. R. Estimating oxygen in the Southern Ocean using Argo temperature and salinity. JGR: Oceans, 123, 4280–4297, https://doi.org/10.1029/2017JC013404, 2018.

1005

Gregor, L., Kok, S., Monteiro, P. M. S. Empirical methods for the estimation of Southern Ocean CO_2: Support Vector and Random Forest Regression. Biogeosciences, 14, 5551–5569, https://doi.org/10.5194/bg-14-5551-2017, 2017.

Gregor, L., Lebehot, A. D., Kok, S., Monteiro, P. M. S. A comparative assessment of the uncertainties of global surface 1010   ocean CO2 estimates using a machine-learning ensemble (CSIR-ML6 version 2019a) – Have we hit the wall? Geosci. Model Dev., 12, 5113–5136. https://doi.org/10.5194/gmd-12-5113-2019, 2019.

Grégoire, M., Garçon, V., Garcia, H., Breitburg, D., Isensee, K., Oschlies, A., Telszewski, M., Barth, A., Bittig, H.C., Carstensen, J., Carval, T., Chai, F., Chavez, F., Conley, D., Coppola, L., Crowe, S., Currie, K., Dai, M., Deflandre, B., 1015   Dewitte, B., Diaz, R., Garcia-Robledo, E., Gilbert, D., Giorgetti, A., Glud, R., Gutierrez, D., Hosoda, S., Ishii, M., Jacinto, G., Langdon, C., Lauvset, S.K., Levin, L. A., Limburg, K. E., Mehrtens, H., Montes, I., Naqvi, W., Paulmier, A., Pfeil, B., Pitcher, G., Pouliquen, S., Rabalais, N., Rabouille, C., Recape, V., Roman, M., Rose, K., Rudnick, D., Rummer, J., Schmechtig, C., Schmidtko, S., Seibel, B., Slomp, C., Sumalia, U. R., Tanhua, T., Thierry, V., Uchida, H., Wanninkhof, R., Yasuhara, M. A Global Ocean Oxygen Database and Atlas for Assessing and Predicting Deoxygenation and Ocean Health in 1020   the Open and Coastal Ocean. Front. Mar. Sci. 8, 724913. https://doi.org/10.3389/fmars.2021.724913, 2021.

Gregor, L., Gruber, N. OceanSODA-ETHZ: a global gridded data set of the surface ocean carbonate system for seasonal to decadal studies of ocean acidification. Earth Syst. Sci. Data, 13, 777–808, https://doi.org/10.5194/essd-13-777-2021, 2021.

1025 Gruber, N., Gloor, M., Fan, S.-M., Sarmiento, J. L. Air-sea flux of oxygen estimated from bulk data: Implications For the marine and atmospheric oxygen cycles. Glob. Biogeochem. Cycl., 15, 783–803, https://doi.org/10.1029/2000GB001302, 2001.

Gruber, N. The dynamics of the marine nitrogen cycle and its influence on atmospheric CO_2 variations. In The ocean carbon cycle and climate. Springer, Dordrecht, 97–148, 2004.

1030

Gruber, N., Doney, S., Emerson, S., Gilbert, D., Kobayashi, T., Körtzinger, A., Johnson, G., Johnson, K., Riser, S., and Ulloa, O.: Adding oxygen to Argo: Developing a global in-situ observatory for ocean deoxygenation and biogeochemistry. In: Proceedings of OceanObs'09: Sustained Ocean Observations and Information for Society, Venice, Italy, 21–25
1035 September 2009, ESA Publication WPP-306, Eds.: Hall, J., Harrison, D., and Stammer, D., https://doi.org/10.5270/OceanObs09.cwp.39, 2010.

Helm, K. P., Bindoff, N. L., Church, J. A. Observed decreases in oxygen content of the global ocean. Geophys. Res. Lett. 38, 1–6, https://doi.org/10.1029/2011GL049513, 2011.

1040

Ito, T., Minobe, S., Long, M. C., Deutsch, C. Upper ocean O_2 trends: 1958–2015. Geophysical Research Letters 44, 4214–4223, https://doi.org/10.1002/2017GL073613, 2017.

Johnson, K. S., Plant, J. N., Riser, S. C., Gilbert, D. Air oxygen calibration of oxygen optodes on a profiling float array. J.
1045 Atmos. Oce. Technol. 32, 2160–2172, https://doi.org/10.1175/JTECH-D-15-0101.1, 2015.

Johnson, K., Claustre, H. Bringing biogeochemistry into the Argo age. Eos 97, https://doi.org/10.1029/2016EO062427, 2016.

1050 Johnson, K. S., Plant, J. N., Coletti, L. J., Jannasch, H. W., Sakamoto, C. M., Riser, S. C., Swift, D. D., Williams, N. L., Boss, E., Haëntjens, N., Talley, L. D., Sarmiento, J. L. Biogeochemical sensor performance in the SOCCOM profiling float array. JGR: Oceans, 122, 6416–6436. https://doi.org/10.1002/2017JC012838, 2017.

Johnson, K. S., Riser, S. C., Ravichandran, M. Oxygen variability controls denitrification in the Bay of Bengal oxygen
1055 minimum zone. Geophys. Res. Lett., 46, 804–811, https://doi.org/10.1029/2018GL079881, 2019.

Johnson, K. S., Bif, M. B. Constraint on net primary productivity of the global ocean by Argo oxygen measurements. Nature Geoscience, 14, 769–774, https://doi.org/10.1038/s41561-021-00807-z, 2021.

1060 Jonsson, B. F., Doney, S. C., Dunne, J., Bender, M. Evaluation of the Southern Ocean O_2/Ar-based NCP estimates in a model framework. Journal of Geophysical Research: Biogeosciences, 118, 385–399, https://doi.org/10.1002/jgrg.20032, 2013.

Keeling, R. F., Arne, K., Gruber, N. Ocean Deoxygenation in a Warming World. Ann. Rev. Mar. Sci. 2, 199–229,
1065 https://doi.org/10.1146/annurev.marine.010908.163855, 2010.

Keppler, L., Landschützer, P., Gruber, N., Lauvset, S. K., Stemmler, I. Seasonal carbon dynamics in the near-global ocean. Glob. Biogeochem. Cycl., 34, e2020GB006571, https://doi.org/10.1029/2020GB006571, 2020.

1070   Keppler, L., Landschützer, P., Lauvset, S. K., Gruber, N. Recent trends and variability in the oceanic storage of dissolved inorganic carbon. Under review for Glob. Biogeochem. Cycl.

Key, R.M., A. Olsen, S. van Heuven, S. K. Lauvset, A. Velo, X. Lin, C. Schirnick, A. Kozyr, T. Tanhua, M. Hoppema, S. Jutterström, R. Steinfeldt, E. Jeansson, M. Ishii, F. F. Perez, and T. Suzuki. Global Ocean Data Analysis Project, Version 2
1075   (GLODAPv2), ORNL/CDIAC-162, NDP-093. Carbon Dioxide Information Analysis Center, Oak Ridge National Laboratory, US Department of Energy, Oak Ridge, Tennessee. https://doi.org/10.3334/CDIAC/OTG.NDP093_GLODAPv2, 2015.

Körtzinger A., Schimanski J., Send U., Wallace D. The ocean takes a deep breath. Science 306, 1337,
1080   https://doi.org/10.1126/science.1102557, 2004.

Körtzinger, A., Schimanski, J., Send, U. High Quality Oxygen Measurements from Profiling Floats: A Promising New Technique, J. Atmos. Ocean. Tech., 22, 302–308, doi:10.1175/JTECH1701.1, 2005.

1085   Kwiatkowski, L., Torres, O., Bopp, L., Aumont, O., Chamberlain, M., Christian, J., Dunne, J., Gehlen, M., Ilyina, T., John, J., Lenton, A., Li, H., Lovenduski, N., Orr, J., Palmieri, J., Schwinger, J., Séférian, R., Stock, C., Tagliabue, A., Takano, Y., Tjiputra, J., Toyama, K., Tsujino, H., Watanabe, M., Yamamoto, A., Yool, A., Ziehn, T. Twenty-first century ocean warming, acidification, deoxygenation, and upper ocean nutrient decline from CMIP6 model projections. Biogeosciences 17, 3439–3470, https://doi.org/10.5194/bg-2020-16, 2020.
1090

Landschützer, P., Gruber, N., Bakker, D. C. E., Schuster, U. Recent variability of the global ocean carbon sink. Global Biogeochem. Cycles, 28, 927–949, https://doi.org/10.1002/2014GB004853, 2014.

Langdon, C. Determination of Dissolved Oxygen in Seaweater By Winkler Titration using Amperometric Technique. In *The*
1095   *GO-SHIP Repeat Hydrography Manual: A Collection of Expert Reports and Guidelines*. Version 1, (eds. Hood, E.M., C.L. Sabine, and B.M. Sloyan). 18pp. (IOCCP Report Number 14; ICPO Publication Series Number 134). https://doi.org/10.25607/OBP-1350, 2010.

Lauvset, S. K., Key, R. M., Olsen, A., Van Heuven, S., Velo, A., Lin, X., et al. A new global interior ocean mapped
1100   climatology: The 1× 1 GLODAP version 2. Earth System Science Data, 8(2), 325–340, https://doi.org/10.5194/essd-8-325-2016, 2016.

Lauvset, S. K., Lange, N., Tanhua, T., Bittig, H. C., Olsen, A., Kozyr, A., et al. GLODAPv2. 2022: the latest version of the global interior ocean biogeochemical data product. Earth System Science Data, 14(12), 5543-5572,
1105   https://doi.org/10.5194/essd-14-5543-2022, 2022.

Limburg, K. E., Breitburg, D., Swaney, D. P., Jacinto, G. Ocean deoxygenation: A primer. One Earth, 2, 24–29, https://doi.org/10.1016/j.oneear.2020.01.001, 2020.

1110   Luz, B. Barkan, E. Assessment of oceanic productivity with the triple-isotope composition of dissolved oxygen. Science 288, 2028–2031, 2000.

Lyman, J. M., Johnson, G. C. Global High-Resolution Random Forest Regression Maps of Ocean Heat Content Anomalies Using in Situ and Satellite Data. J. Atmos. Oce. Technol. https://doi.org/10.1175/JTECH-D-22-0058.1, 2023.
1115

Maurer, T. L., Plant, J. N., Johnson, K. S. Delayed-Mode Quality Control of Oxygen, Nitrate, and pH Data on SOCCOM Biogeochemical Profiling Floats. Front. Mar. Sci., 8, https://doi.org/10.3389/fmars.2021.683207, 2021.

McDougall, T. J., Barker, P. M. Getting started with TEOS-10 and the Gibbs Seawater (GSW) oceanographic toolbox. Scor/Iapso WG, 127, 1–28, 2011.

Nicholson, D. P., & Feen, M. L. Air calibration of an oxygen optode on an underwater glider. Limnol. Oceanogr.: Methods, 15, 495–502. https://doi.org/10.1002/lom3.10177, 2017.

NOAA National Geophysical Data Center. 2-minute Gridded Global Relief Data (ETOPO2) v2. NOAA National Centers for Environmental Information. https://doi.org/10.7289/V5J1012Q. 2006. Accessed 7/30/2021.

Olsen, A., R. M. Key, S. van Heuven, S. K. Lauvset, A. Velo, X. Lin, C. Schirnick, A. Kozyr, T. Tanhua, M. Hoppema, S. Jutterström, R. Steinfeldt, E. Jeansson, M. Ishii, F. F. Pérez and T. Suzuki. The Global Ocean Data Analysis Project version 2 (GLODAPv2) – an internally consistent data product for the world ocean, Earth Syst. Sci. Data, 8, 297–323, doi:10.5194/essd-8-297-2016, 2016

Oschlies, A., Duteil, O., Getzlaff, J., Koeve, W., Landolfi, A., Schmidtko, S. Patterns of deoxygenation: sensitivity to natural and anthropogenic drivers. Phil Trans. Royal Soc. A, 375, 20160325, https://doi.org/10.1098/rsta.2016.0325, 2017.

Oschlies, A., Brandt, P., Stramma, L., Schmidtko, S. Drivers and mechanisms of ocean deoxygenation. Nature Geoscience, 11, 467–473. https://doi.org/10.1038/s41561-018-0152-2, 2018.

Piron, A., Thierry, V., Mercier, H., Caniaux, G. Argo float observations of basin-scale deep convection in the Irminger sea during winter 2011–2012. Deep Sea Res. I, 109, 76–90, https://doi.org/10.1016/j.dsr.2015.12.012, 2016.

Piron, A., Thierry, V., Mercier, H., and Caniaux, G. Gyre-scale deep convection in the subpolar North Atlantic Ocean during winter 2014–2015. Geophys. Res. Lett., 44, 1439–1447, https://doi.org/10.1002/2016GL071895, 2017.

Pörtner, H. O., Farrell, A. P. Physiology and climate change. Science, 322, 690–692, https://doi.org/10.1126/science.1163156, 2008.

Reuer, M. K., Barnett, B. A., Bender, M. L., Falkowski, P. G., Hendricks, M. B. New estimates of Southern Ocean biological production rates from O_2/Ar ratios and the triple isotope composition of O_2. Deep Sea Res. I, 54, 951–974, https://doi.org/10.1016/j.dsr.2007.02.007, 2007.

Ritter, R., Landschützer, P., Gruber, N., Fay, A. R., Iida, Y., Jones, S., Zeng, J. Observation-Based Trends of the Southern Ocean Carbon Sink, Geophys. Res. Lett., 2, 339–348, https://doi.org/10.1002/2017GL074837, 2017.

Roemmich, D., Gilson, J. The 2004-2008 mean and annual cycle of temperature, salinity, and steric height in the global ocean from the Argo Program. Progress in Oceanography, 82, 81–100. https://doi.org/10.1016/j.pocean.2009.03.004, 2009.

Roemmich, D., Alford, M. H., Claustre, H., Johnson, K. S., et al. On the future of Argo: A global, full-depth, multi-disciplinary array. Frontiers in Marine Science, 6, 1–28. https://doi.org/10.3389/fmars.2019.00439, 2019.

Roemmich, D., L. Talley, N. Zilberman, E. Osborne, K.S. Johnson, L. Barbero, H.C. Bittig, N. Briggs, A.J. Fassbender, G.C. Johnson, B.A. King, E. McDonagh, S. Purkey, S. Riser, T. Suga, Y. Takeshita, V. Thierry, and S. Wijffels. The technological, scientific, and sociological revolution of global subsurface ocean observing. In *Frontiers in Ocean Observing: Documenting Ecosystems, Understanding Environmental Changes, Forecasting Hazards*. Eds. E.S. Kappel, S.K. Juniper, S. Seeyave, E. Smith, M. Visbeck, 2–8. A Supplement to Oceanography 34, https://doi.org/10.5670/oceanog.2021.supplement.02-02, 2021.

Sampaio, E., Santos, C., Rosa, I. C., Ferreira, V., Pörtner, H., Duarte, C. M., et al. Impacts of hypoxic events surpass those of future ocean warming and acidification. Nature Ecology & Evolution, 5, 311–321. https://doi.org/10.1038/s41559-020-01370-3, 2021.

Sauzède, R., Claustre, H., Jamet, C., Uitz, J., Ras, J., Mignot, A., d'Ortenzio, F. Retrieving the vertical distribution of chlorophyll a concentration and phytoplankton community composition from in situ fluorescence profiles: A method based on a neural network with potential for global-scale applications. JGR: Oceans, 120, 451–470, https://doi.org/10.1002/2014JC010355, 2015.

Sauzède, R., Claustre, H., Uitz, J., Jamet, C., Dall'Olmo, G., d'Ortenzio, F., Gentili, B., Poteau, A., Schmechtig, C. A neural network based method for merging ocean color and Argo data to extend surface bio optical properties to depth: Retrieval of the particulate backscattering coefficient. JGR: Oceans, 121, 2552–2571, https://doi.org/10.1002/2015JC011408, 2016.

Sauzède, R., Claustre, H., Pannimpullath, R., Uitz, J., Guinehut, S. New Global Vertical Distribution of Gridded Particulate Organic Carbon and Chlorophyll Concentration Using Machine Learning for CMEMs. In 9th EuroGOOS International conference, https://hal.archives-ouvertes.fr/hal-03335370, 2021.

Sarma V. V. S. S., Udaya Bhaskar T. V. S. Ventilation of oxygen to oxygen minimum zone due to anticyclonic eddies in the Bay of Bengal. J. Geophys. Res. Biogeosci. 123, 2145–2153, https://doi.org/10.1029/2018JG004447, 2018.

Sarmiento, J.L., Gruber, N. Ocean Biogeochemical Dynamics. Princeton University Press, Princeton, NJ, 2006.

Schofield, O., A. Fassbender, M. Hood, K. Hill, K. Johnson. A global ocean biogeochemical observatory becomes a reality, Eos, 103, https://doi.org/10.1029/2022EO220149, 2022.

Schmidtko, S., Stramma, L., Visbeck, M. Decline in global oceanic oxygen content during the past five decades. Nature, 542, https://doi.org/10.1038/nature21399, 335–339, 2017.

Sharp, J. D., Fassbender, A. J., Carter, B. R., Johnson, G. C., Schultz, C., Dunne, J. P. GOBAI-O2: A Global Gridded Monthly Dataset of Ocean Interior Dissolved Oxygen Concentrations Based on Shipboard and Autonomous Observations (NCEI Accession 0259304). V2.0. NOAA National Centers for Environmental Information. Dataset. https://doi.org/10.25921/z72m-yz67, 2023.

Sharp, Jonathan D. GOBAI-O2 Training Data [Data set]. Zenodo. https://doi.org/10.5281/zenodo.7747237, 2023a.

Sharp, Jonathan D. GOBAI-O2 Algorithms. Zenodo. https://doi.org/10.5281/zenodo.7747309, 2023b.

Stramma, L., Schmidtko, S. Global evidence of ocean deoxygenation. In Ocean Deoxygenation: Everyone's Problem. Eds. D. Laffoley, J. M. Baxter. 25-26. IUCN. Gland, Switzerland, 2019.

Stramma, L., Schmidtko, S. Spatial and Temporal Variability of Oceanic Oxygen Changes and Underlying Trends, Atmos.-Ocean. 59, 122–132, https://doi.org/10.1080/07055900.2021.1905601, 2021.

Stukel MR, Ducklow HW. Stirring up the biological pump: vertical mixing and carbon export in the Southern Ocean. Glob. Biogeochem. Cycles 31, 1420–1434, https://doi.org/10.1002/2017GB005652, 2017.

Takeshita, Y., Martz, T. R., Johnson, K. S., Plant, J. N., Gilbert, D., Riser, S. C., Neill, C., Tilbrook, B. A climatology-based quality control procedure for profiling float oxygen data. JGR: Oceans, 118, 5640–5650. https://doi.org/10.1002/jgrc.20399, 2013.

Talley, L. D. Descriptive physical oceanography: an introduction. Academic press, 2011.

1220 Testor, P., de Young, B., Rudnick, D. L., Glenn, S., Hayes, D., Lee, C. L., et al. OceanGliders: A component of the integrated GOOS. Front. Mar. Sci. 6, 422, 10.3389/fmars.2019.00422, 2019.

Udaya Bhaskar, T. V. S., Sarma, V. V. S. S., Pavan Kumar, J. Potential mechanisms responsible for spatial variability in intensity and thickness of oxygen minimum zone in the Bay of Bengal. JGR: Biogeosciences 126,
1225 https://doi.org/10.1029/2021JG006341, 2021.

Wang Z., Garcia H. E., Boyer T. P., Reagan J., Cebrian J. Controlling factors of the climatological annual cycle of the surface mixed layer oxygen content: A global view. Front. Mar. Sci. 9:1001095. https://doi.org/10.3389/fmars.2022.1001095, 2022
1230
Winkler, L. W. Die Bestimmung des imWasser gelösten Sauerstoffes. Chem. Ber. 21, 2843–2855. 10.1002/cber.188802102122, 1888.

Wolf M. K., Hamme R. C., Gilbert D., Yashayaev I., Thierry V. Oxygen saturation surrounding deep water formation events
1235 in the Labrador Sea from Argo-O_2 data. Glob. Biogeochem. Cycles 32, 635–653, https://doi.org/10.1002/2017GB005829, 2018.

Yang, B., Emerson, S. R., and Bushinsky, S. M. Annual net community production in the subtropical Pacific Ocean from in situ oxygen measurements on profiling floats. Glob. Biogeochem. Cycl. 31, 728–744,
1240 https://doi.org/10.1002/2016GB005545, 2017.